Duration of the Petermann Orogeny from coupled diffusion and phase equilibria modelling

Alec Walsh

Centre for Tectonic Resources and Exploration
Department of Geology and Geophysics
School of Earth and Environmental Sciences
University of Adelaide, South Australia
alec.walsh@student.adelaide.edu.au

25th October, 2010

Table of Contents

Duration of the Petermann Orogeny from coupled diffusion and phase equilibria modelling

Alec Walsh

Centre for Tectonic Resources and Exploration
Department of Geology and Geophysics
School of Earth and Environmental Sciences
University of Adelaide, South Australia
alec.walsh@student.adelaide.edu.au

Abstract

The Ediacaran to Cambrian (600-500 Ma) intraplate Petermann Orogeny significantly affected the crustal architecture of Central Australia, resulting in the exhumation of the Musgrave Province from beneath the Centralian Superbasin. In the western Musgrave Province response to intensive deformation is variable, with pervasive mylonitic reworking and localised migmitisation in the western Mann Ranges, and discrete mylonitisation in the eastern Mann Ranges. The duration of this period of intraplate orogenesis is a currently debated topic. Ti-in-zircon thermometry coupled with SHRIMP U-Pb zircon geochronology indicate that peak temperatures of 733±23°C in the western Mann Ranges occurred at *circa* 540 Ma. Combined diffusion-cooling modelling, U-Pb rutile and titanite isotopic data and calculated phase equilibria of recrystallised metagranites from the Cockburn Shear Zone and kyanite-bearing mylonites from the Mt. Charles Thrust indicate exhumation driven cooling from peak *P-T* conditions of 12-14 kbars and 700-750°C to 6-7 kbars and 550-600°C at *c.* 500 Ma occurred at a rate of 3.75-5.6°C/ My. These results indicate a slow-cooling and long-lived thermal regime and additionally suggests that final exhumation of the Musgrave

Province had not occurred by *c*. 500 Ma, much younger than previously estimated. These findings suggest that granulite-facies metamorphism in the Musgrave Province was regional and that other factors such as fluid, control the variations in style of structural reworking. This study lends support to the notion that the intraplate Petermann Orogeny was long-lived and does not advocate short-lived orogenesis or the theory that shear heating is the driving force for metamorphism.

Key words: Musgrave Province, Petermann Orogeny, intraplate deformation, phase equilibria, rutile, titanite, diffusion cooling

Introduction

Intraplate orogens are produced at considerable distances from active plate margins and therefore their evolution cannot be immediately explained by conventional plate tectonic models. Central Australia records remarkable examples of intraplate orogenesis. The 600-530 Ma Petermann Orogeny and the 450-300 Ma Alice Springs Orogeny are both major, large-scale intraplate events that define the crustal architecture of the interior of the Australian plate (Lambeck & Burgess 1992, Lindsay & Leven 1996, Korsch *et al.* 1998, Sandiford & Hand 1998, Hand & Sandiford 1999, Scrimgeour & Close 1999, Aitken & Betts 2009a, 2009b) and were responsible for the exhumation of vast tracts of crystalline basement from beneath the formerly contiguous Centralian Superbasin (Walter *et al.* 1995, Hand & Sandiford 1999, Sandiford *et al.* 2001). In the case of the Petermann Orogeny, exhumation of crystalline rocks of the Mesoproterozoic Musgrave Province involved the generation of >100-km-scale basement-cored nappe structures (Flöttmann *et al.* 2004).

The Petermann Orogeny is well-exposed and has been the subject of numerous studies (Camacho *et al.* 1997, White & Clarke 1997, Scrimgeour & Close 1999, Camacho *et al.* 2001, Aitken *et al.* 2009, Camacho *et al.* 2009, Gregory *et al.* 2009, Raimondo *et al.* 2009, Aitken & Betts 2009a, 2009b, Raimondo *et al.* 2010). However, the evolution of the Petermann Orogeny, specifically the duration, rates and physical and thermal conditions of the event, remains contentious or relatively poorly understood. The Petermann Orogeny is additionally intriguing as high-pressure, low geothermal gradient (~20 °C km^{-1}) metamorphic rocks (near-eclogites) that are not the consequence of subduction were generated (Ellis & Maboko 1992). The preservation of 'cold' metamorphic rocks suggests at face value that rapid exhumation occurred, contrasting with the generally held perception that intraplate orogenesis involves slow exhumation. Rocks affected by the Petermann Orogeny thus provide an ideal natural laboratory to study intraplate orogenesis.

Two contrasting views exist regarding the rates and duration of the Petermann Orogeny (Camacho *et al.* 2009, Raimondo *et al.* 2009, 2010). Camacho *et al.* (2001) suggested that near-eclogite facies rocks formed by localised shear heating over very short durations and lateral distance. Camacho *et al* (2009) expanded on this concept to suggest that shear heating was the thermal driving mechanism for the Petermann Orogeny. The implication is that the duration of metamorphism/tectonism in any one part of the orogen is extremely short-lived (*c.* 1 My.) yet involved very substantial exhumation (> 40 km). By contrast, Raimondo *et al.* (2009, 2010) proposes that the Petermann Orogeny is characterised by intracontinental channel-flow. As a result deformation is locally pervasive and migmatitic (e.g. Scrimgeour et al 1999). This style of deformation necessitates a hot, weak crust and implies that duration of metamorphism is far longer (*c.* > 30 M.y.) (Pysklywec & Beaumont 2004) and geothermal gradients are far higher than suggested by Camacho *et al.* (2009).

In order to more completely understand the characteristics of intraplate orogeny, this study presents a detailed analysis of the *P-T-time* evolution of rocks that underwent intraplate reworking during the Petermann Orogeny. This study focuses on a suite of samples spatially located approximately midway between the sites of Camacho *et al*. (2001, 2009) and Raimondo *et al.* (2009, 2010). An approach integrating Sensitive High-Resolution Ion Microprobe (SHRIMP) and Laser Ablation – Inductively Coupled Mass Spectrometry (LA-ICPMS) geochronology, trace element thermometry, calculated metamorphic phase diagrams and diffusion-cooling modelling is used to provide constraints on the time-integrated thermal and physical conditions of orogeny. The results of this study are used to assess the Camacho *et al*. (2001, 2009) and Raimondo *et al*. (2009, 2010) 'end-members' currently explaining the evolution of the Petermann Orogeny. In a broader sense, the approach and methodologies applied here are relevant to understanding other examples of intraplate orogeny.

Geological setting

The Musgrave Province is a Meso-Neoproterozoic basement inlier that forms an east-west trending gravity high that straddles the Northern Territory, South Australian and Western Australian borders (Wade *et al*., 2008) (Figure 1). It is bounded by the Amadeus Basin to the north, and the Officer Basin to the south, which once comprised the Centralian Superbasin ((Lindsay *et al.* 1987, Walter *et al.* 1995).

The Musgrave Province exposes a variety of 1600-1300 Ma ortho-gneisses, 1200-1140 Ma felsic magmatic rocks, 1080-1026 Ma mafic and ultramafic intrusions and mafic-felsic volcanics, that preserve a complex deformational, metamorphic and magmatic history (Glikson 1995, Sun 1996, Edgoose 2004, Wade *et al.* 2008, Evins *et al.* 2010, Smithies *et al.* 2010). The oldest, approximately 1600 Ma, rocks in the Musgrave Province appear to be

confined to the eastern Musgrave Province (Ailsa Woodhouse, Primary and Industry Resources South Australia. personal communication 2010). 1345-1290 Ma magmatism and metamorphism is preserved in the west Musgrave Province as the Mt West Orogeny (Evins *et al.* 2010, Smithies *et al.* 2010). The dominant metamorphic expression of the Musgrave Province is a result of the 1230-1150 Ma Musgrave Orogeny, during which temperature-pressure conditions of > 850 °C and 7-8 kbars were reached, causing regionally extensive granulite facies metamorphism (Glikson 1996, White *et al.* 1999, White *et al.* 2002, Wade *et al.* 2008, Kelsey *et al.* 2009, Kelsey *et al.* 2010, Smithies *et al.* 2010). Coeval with the Musgrave Orogeny was voluminous magmatism, manifest as the Pitjantjatjara Supersuite granitoids (Maboko *et al.* 1992, White *et al.* 1999, Edgoose 2004, Evins *et al.* 2010, Smithies *et al.* 2010). Subsequent to the Musgrave Orogeny, layered mafic-ultramafic dikes and intrusions of the Giles Event were emplaced at *c.* 1080 Ma (Glikson 1996, Sun 1996, Evins *et al.* 2010), followed by the emplacement and extrusion of felsic granites and volcanics between *c.* 1075 and 1026 Ma (Sun 1996, Wade *et al.* 2008, Evins *et al.* 2010). The emplacement of the Alcurra and Amata mafic dike swarms at *c.* 1000 Ma and *c.* 830 Ma are the only recorded events until the onset of the Petermann Orogeny (Zhao *et al.* 1994, Glikson 1996, Sun 1996).

The onset of the Petermann Orogeny at *c.* 600 Ma is constrained by the influx of basement-derived sediments into the Officer Basin (Wade *et al.* 2005). The Petermann Orogeny exhumed the Musgrave Province from beneath the Centralian Superbasin (Walter *et al.* 1995, Hand & Sandiford 1999), and led to the present day E-W architecture of the Musgrave Province (Wade *et al.* 2008). Deformation was focused on the northern margin of the exposed Musgrave Province, producing a series of major E-W trending fault structures that extend up to 40 km depth and displace the Moho (Korsch *et al.* 1998). The most significant of these structures are the Mann Fault and the Woodroffe Thrust. The latter of these is a shallowly

south-dipping mylonite and psuedotachylyte zone up to 3 km thick that offsets the Moho by ~20 km (Lambeck & Burgess 1992, Camacho & Fanning 1995, Aitken *et al.* 2009), and created a large gravitational gradient that is maintained today (Sandiford & Hand 1998, Aitken *et al.* 2009). Top to the north thrusting coupled with lower crustal extrusion along the Woodroffe Thrust facilitated the exhumation of high grade lower crustal rocks from approximately 40 km depth and the emplacement of a broad crustal wedge (Camacho *et al.* 1997, Scrimgeour & Close 1999, Raimondo *et al.* 2009, 2010). The core of the Petermann Orogen is exposed in an E-W orientation in the central Musgrave Province between the Mann Fault and Woodroffe Thrust, where the rocks express variable degrees of tectonic reworking (Wade *et al.* 2008). Reworking is expressed as discrete shear zones that range in width from cm to km scale and have corresponding strike lengths up to hundreds of km (Camacho *et al.* 1997, Wade *et al.* 2008). In regions such as the western Mann ranges, Petermann-aged deformation is expressed as a large-scale pervasive migmatitic fabric that has overprinted earlier structural fabrics (Scrimgeour & Close 1999). Syn-kinematic low-angle shear fabrics, which record opposing kinematics along a north-south transect, occur on a regional scale throughout the western Musgrave Province (Raimondo *et al.* 2009, 2010). Mylonitic fabrics from shear zones in the eastern Mann Ranges also provide evidence for opposing kinematics, with top to the south shear sense of Petermann age (Hallet 2007).

Sequential cross section restorations indicate that north-directed shortening during the Petermann Orogeny exceeded 100 km and was accommodated by significant crustal thickening (Flöttmann *et al.* 2004). This is supported by thermobarometric constraints from the exposed orogenic core between the Woodroffe Thrust and the Mann Fault, with the highest pressure-temperature conditions of ~12-14 kbar and 700-750 ºC attained immediately north of the Mann Fault (Camacho *et al.* 1997, White & Clarke 1997, Scrimgeour & Close 1999, Gregory *et al.* 2009, Raimondo *et al.* 2010). The eastern core of the orogen records up

to sub-eclogitic facies mineral assemblages in the Davenport Shear Zone that formed at between 12-14 kbar and temperatures around 600-650 °C (Camacho *et al*., 1997). Westward, the core of the orogen appears to be hotter, with temps around 700-750 °C and pressures equal to or less than the eastern core (Raimondo *et al.* 2010). Metamorphic grade decreases toward the foreland to the north, where *P-T* conditions of ~6-7 kbar and ~600-650 ºC are recorded north of the Woodroffe thrust (Scrimgeour & Close 1999).

Migmatitic shear zones and lower grade mylonitic zones in the Mann Ranges locally and discretely overprint the high-grade mylonitic fabrics and are presumed to be associated with exhumation of the core of the orogen (Scrimgeour & Close 1999). Exhumation is estimated to have occurred quite rapidly over a ~20 m.y. period at rates of *c.* 0.2-1.5 mm/yr, which corresponds to a moderately fast cooling rate of *c.* 3-20 ºC/m.y (Camacho *et al.* 1997).

The age of Petermann orogenesis is relatively well constrained in selected regions (Figure 2; Table 1). U-Pb dating of metamorphic zircon and titanite from the Bates region suggests that peak conditions occurred at *c.* 570 Ma (Raimondo *et al.* 2009, 2010). In the western Mann Ranges, Gregory *et al.* (2009) reports U-Pb allanite and zircon ages of 559±6 Ma and 555±7 Ma respectively, which is consistent with other estimates from the region (Scrimgeour & Close 1999, Pfitzner 2009). Further to the east, age estimates for peak metamorphism are sparse. A U-Pb monazite chemical age of 580±22 Ma from the Angatja region (eastern Mann Ranges) providing the only constraint on Petermann aged reworking (Hallet 2007). Synkinematic biotite and muscovite growth from the Woodroffe Thrust at 530 Ma is the youngest recorded deformation and defines the cessation of exhumation (Camacho & Fanning 1995).

Petrographic descriptions

High-grade metamorphic assemblages from metagranitic and metapelitic rocks and metamorphosed mafic dykes in the Musgrave Province are host to abundant monazite, zircon, titanite and rutile and are therefore are prospective samples for geochronology, with the aim to constrain the age of peak metamorphic conditions. These metamorphic assemblages are also very conducive to calculated phase diagram analysis, which provides constraints on the physical conditions of metamorphism. Several samples are also conducive for diffusion modelling as they host appropriate garnet-biotite or garnet-hornblende assemblages and textures, useful in constraining the cooling history of the Petermann Orogeny.

Samples used in this study are taken from a wider set of samples collected throughout the Musgrave Province during previous studies. Group 1 samples are from the eastern Mann ranges and are dominantly fine-grained mylonites and have been subject to the studies of Hallet *et al* (2007) (prefix LH) and Scrimgeour & Close (1999) (numbered, no prefix). Additional samples were collected by D. Kelsey and M. Hand (prefix M or Mann). Group 2 samples are from the western Mann ranges. Samples are dominantly metagranitic or metamorphosed mafic dykes and were collected by Scrimgeour (numbered, no prefix) and Close (prefix DFC). Group 3 samples are from the migmatitic Cockburn Shear Zone (CSZ). Samples are metagranitic gneisses and were collected by Buick (prefix Pe).

This selection of samples defines a large region of the high-grade metamorphic core of the Peterman Orogeny and is representative of regions that record distinct variations in response to deformation during intraplate reworking. Samples from the western Mann Ranges and the CSZ represent regions of pervasive deformation and localised migmitisation. In contrast, samples from the eastern Mann Ranges represent regions of discrete mylonitisation and record no migmitisation. Therefore this suite of samples ensures that constraints on the

physical and thermal conditions and duration of orogenesis are integrated across contrasting structural domains and therefore allows a thorough assessment of the contrasting models proposed for the evolution of the Petermann Orogeny.

In the following descriptions, peak and post-peak assemblages are interpreted based on grain size and microstructural relationships, such as porphyroblasts or coronae. The interpretation of accessory minerals as peak or post-peak is typically difficult, but is crucial for the interpretation of age data.

Group 1- Eastern Mann Ranges

LH16B

Layers of quartz and plagioclase separate layers of hornblende, poikiloblastic garnet (up to 5 mm), clinopyroxene, clinozosite, ilmenite and potassium feldspar (K-feldspar), which results in a gneissic texture (Fig. 3a). Poikiloblastic garnet contains inclusions of quartz and are wrapped by the quartz-plagioclase fabric. Garnet commonly is mantled by coronas of plagioclase and occasionally hornblende. K-feldspar occurs as large euhedral porhyroblasts that are often wrapped by a fabric defined by hornblende, ilmenite and clinozoisite. Hornblende commonly occurs as coronas with plagioclase around garnet, although there are some examples of euhedral grains in the matrix. Accessory zircon and titanite are commonly euhedral grains that occur in the quartz-plagioclase matrix or in direct contact with hornblende. Biotite commonly occurs in strain shadows around garnet. The peak-assemblage is interpreted to comprise garnet, plagioclase, K-feldspar, illmenite, clinozoisite and hornblende, with biotite comprising the post-peak assemblage.

LH114

Porphyrbclastic garnet (up to 2 mm) and K-feldspar (up to 1 mm), exist in a fine-grained matrix of plagioclase, quartz, biotite, clinozoisite and K-feldspar. Layers of plagioclase, quartz and prismatic biotite and clinozoisite grains define a strong mylonitic fabric that wraps garnet and K-feldspar grains (Fig. 3b). Larger anhedral biotite grains occur in strain shadows of both garnet and K-feldspar porphyroblasts. The peak-assemblage is interpreted to comprise garnet, plagioclase, K-feldspar, illmenite, biotite and clinozoisite.

577C

Porphyroblastic garnet (up to 3 mm) and K-feldspar (up to 5mm) occur in a finer grained mylonitic fabric of plagioclase, kyanite, quartz and ilmenite. Coarse-grained garnet commonly have tails of much finer-grained garnet which tail off into the mylonitic fabric. Much finer-grained garnet growth often rims coarse garnet grains and is often in contact with plagioclase. Plagioclase grains commonly contain very fine-grained, fibrous and acicular kyanite (Fig. 3c). Dark, fibrous kyanite and ilmenite, along with fine-grained garnet define a strong foliation that wraps garnet and K-feldspar porphyroclasts (Fig. 3d). The peak-assemblage is interpreted to comprise garnet, plagioclase, K-feldspar, ilmenite, kyanite and biotite.

LH022B

Poikiloblastic garnet (up to 8 mm) grains occur in a mylonitic matrix defined by fine-grained fibrous kyanite, biotite, ilmenite, quartz and K-feldspar. Garnet is heavily fractured and contains abundant inclusions of quartz and K-feldspar and occasionally biotite and ilmenite which more commonly occurs at rims of garnets (Fig. 3e). Rounded monazite grains occurs in the matrix, occasionally at grain boundaries of garnet or biotite and often along fractures in

garnet grains. The peak-assemblage is interpreted to comprise garnet, plagioclase, K-feldspar, ilmenite and biotite.

Group 2- Western Mann Ranges

DFC 387

The rock is dominated by a fine-grained matrix of garnet and clinopyroxene grains (Fig. 3f). Sub-angular to angular porphyroblastic garnet grains up to 1 mm in diameter are commonly surrounded by a double corona of plagioclase then clinopyroxene. Fine-grained (<1.5 mm) clinopyroxene grains are euhedral and are commonly in contact with plagioclase and more rarely with garnet. Plagioclase always occurs in contact with garnet often forming thin coronas around garnet grains. Fine grained (0.5-1 mm) angular rutile is the dominant accessory phase and occur within the matrix and at grain boundaries and along fractures of porhyroblastic garnet and clinopyroxene. The peak-assemblage is interpreted to comprise garnet and clinopyroxene with accessory rutile, plagioclase comprises the post-peak assemblage.

441

Fine grained matrix of garnet and clinopyroxene, quartz and rutile dominates the rock (Fig. 3g). Plagioclase occurs both in the matrix and as coronas. Minerals are generally inclusion free, although garnet sometimes includes rutile, otherwise rutile occurs at grain boundaries. Some rutile is extremely orange rather than opaque. Clinozoisite also occurs at grain boundaries and often in contact with plagioclase. Garnet and clinopyroxene occasionally occur in as aggregates of euhedral grains and are not separated by plagioclase or quartz, probably reflective of peak conditions. The peak-assemblage is interpreted to comprise garnet, quartz and clinopyroxene with accessory rutile, plagioclase and clinozoisite comprise the post-peak assemblage.

542

Fine-grained euhedral clinopyroxene and garnet (up to 3 mm) comprise a matrix with rutile the accessory phase. Garnet and clinopyroxene are commonly inclusion free with only occasional rutile in grain fractures. Some of the larger garnet and clinopyroxene grains do however have inclusion-rich cores (Fig. 3h). Plagioclase growth is restricted forming coronas to garnet aggregates (Fig. 3i). Hornblende grains are anhedral and appear to be contained within larger scale fractures in the rock where fluid flow has promoted the growth of the hydrous phase. Rutile occurs as inclusions in garnet, clinopyroxene and hornblende although more commonly occurs at grain boundaries or in plagioclase moats. The peak-assemblage is interpreted to comprise garnet and clinopyroxene with accessory rutile, plagioclase and hornblende comprises the post-peak assemblage.

532A

Poikiloblastic garnet (up to 5 mm) occur in a finer-grained matrix of clinopyroxene, hornblende, plagioclase, biotite, quartz and K-feldspar, with titanite and ilmenite comprising the accessory phases. Garnet cores are inclusion-rich with quartz, plagioclase and titanite, whereas the rims are relatively inclusion-free (Fig. 3j). Euhedral clinopyroxene grains (3-5 mm) always occur in contact with plagioclase and hornblende. Hornblende is anhedral and slightly elongate, up to 6 mm in length, and almost exclusively forms coronas around garnet poikiloblasts. Titanite is the dominant accessory phase occurring commonly at grain boundaries of hornblende, occasionally with plagioclase. The peak-assemblage is interpreted to comprise garnet, hornblende, biotite, k-feldspar, plagioclase and clinopyroxene with accessory ilmenite and titanite.

DFC507

Poikiloblastic garnet (up to 3 mm) occurs in a fine-grained matrix of biotite, K-feldspar, quartz, clinozoisite and plagioclase with titanite and ilmenite forming the accessory phase. Garnet is always in contact with plagioclase and inclusions are commonly plagioclase and quartz and occasionally titanite and ilmenite (Fig. 3k). Porphyroclastic K-feldspar grains are up to 5 mm, far larger than the surrounding matrix. Titanite growth almost exclusively occurs as coronae on ilmenite (Fig. 3l).

Group 3- Cockburn Shear Zone

Pe24

Coarse-grained garnets (up to 18 mm) and hornblende occur in a fine-grained matrix of quartz, K-feldspar and fine-grained elongate biotite grains define a weak foliation. Titanite and less common rutile and zircon comprise the accessory phases in the assemblage. Garnet poikiloblasts include quartz, K-feldspar and less commonly rutile and titanite (Fig. 3n). Coarse-grained euhedral hornblende (up to 8 mm) contain inclusions of quartz and K-feldspar and less commonly titanite and rutile (Fig. 3m). Titanite inclusions in both garnet and hornblende are randomly orientated (long axis), whereas those in the matrix are orientated parallel to the structural fabric (Fig. 3o). Rutile occurs as inclusions in garnet and hornblende but is restricted to fractures within the grains. Zircon occurs predominantly at grain boundaries of both poikiloblastic garnet and hornblende although occasionally occurs in the matrix, generally orientated parallel to the foliation. Elongate hornblende and/or biotite grains occur in strain shadows around garnet grains. Garnet, hornblende, biotite, K-feldspar and quartz comprise the peak assemblage with accessory rutile, zircon and titanite.

Pe17

Fine-grained clinopyroxene (up to 2mm), hornblende, garnet (up to 1mm) and plagioclase form the peak assemblage, with titanite, rutile and ilmenite forming the accessory phases. Clinopyroxene habits as aggregates of fine-grained euhedral grains and almost exclusively occurs in contact with hornblende, occasionally with garnet and rarely with plagioclase. Garnet occurs as aggregates of fine, inclusion-free grains. They occasionally form coronas around clinopyroxene and is always found in contact with plagioclase (Fig. 3p). Hornblende occurs as anhedral grains that almost exclusively form coronas around clinopyroxene (Fig. 3q). Euhedral rutile grains range in colour from yellow to dark brown and occur at grain boundaries of garnet. Rutile is commonly rimmed by titanite, particularly when included in garnet.

Pe9

Fine-grained poikiloblastic garnets (up to 3mm), clinopyroxene, quartz, plagioclase, hornblende and rutile form the peak assemblage, with accessory titanite. Garnet has common inclusions of randomly orientated plagioclase, quartz and clinozoisite, and it occurs in contact with plagioclase and hornblende (Fig. 3r). Euhedral clinopyroxene grains are commonly inclusion rich. Titanite growth is texturally late with respect to the peak assemblage. It almost exclusively forms coronas around rutile and ilmenite grains and titanite growth is purely controlled by the presence of either of these oxides (Fig. 3t).

Methods

Electron Microprobe (EMP) mineral analysis was undertaken to obtain mineral compositions data and elemental maps, with the aim to constrain *P-T* conditions of metamorphism, constrain cooling via elemental zonation and construct bulk compositions for phase diagram

calculations. Laser Ablation-Inductively Coupled Plasma Mass Spectrometer (LA-ICPMS) and Sensitive-High Resolution Ion Microprobe (SHRIMP) analysis was undertaken to obtain U-Pb age data and trace element data, with the aim of constraining timing of high-grade metamorphism, the timing of the retrograde evolution of the Petermann Orogeny and the thermal conditions associated with accessory mineral growth during intraplate deformation.

Mineral Chemistry and Elemental mapping

Mineral chemistries were obtained at the University of Adelaide via electron microprobe analysis using a Cameca SX51 electron microprobe (EMP) equipped with four wavelength-dispersive spectrometers, and using a beam current of 20 nA and accelerating voltage of 20 kv. Representative mineral analyses of each petrological group are provided in Table 2. Elemental mapping was conducted on the Cameca SX51 EMP utilising beam conditions of 100 nA and 15 kv. Elemental mapping was conducted to identify the distribution of particular minerals in addition to highlighting internal compositional zoning.

In-situ LA-ICPMS U-Pb geochronology

Sample preparation

Monazite samples were selected based on the presence and abundance of monazite in thin section as well as the spatial field location of the sample. Corresponding thin sections of selected samples were adequately polished and then coated in carbon prior to imaging. Individual monazites were identified and imaged for internal zonation and morphology using backscattered electron imaging techniques on the Philips XL30 SEM equipped with EDAX electron dispersive spectrometers.

LA-ICPMS operating procedures and data reduction

U-Th-Pb analysis of monazite was conducted using an Agilent 7500cs ICPMS coupled with a New Wave 213 nm Nd-YAG laser. Ablation was performed in a helium atmosphere, with a beam diameter of 12 μm, repetition rate of 5 Hz and laser intensity of 75%. Total acquisition time for each analysis was 90 seconds, and involved 40 seconds of background measurement, 10 seconds for beam and crystal stabilisation, and 40 seconds of sample ablation. U-Pb fractionation was corrected for using the external monazite standard 440, and accuracy was measured repeatedly by analysing internal monazite standards 222 and Madel. Data reduction was completed using GLITTER (Van Achterbergh. *et al*., 2001). Common Pb was not corrected for in age calculations due the unresolvable signal interference of ^{204}Hg with the ^{204}Pb isotope peak. The spectrometry signal for ^{204}Pb was observed for anomalous peaks in an attempt to compensate for this.

SHRIMP and LA-ICPMS U-Pb-Th geochronology

Samples were selected for U-Pb geochronological analysis based on the presence of either rutile, titanite or zircon, and their occurrence in petrographically suitable relationships. The rationale behind undertaking zircon and titanite U-Pb geochronology follows the success of previous studies of Pfitzner (2009) and Raimondo *et al*. (2009; 2010) in constraining the timing of peak metamorphism during Petermann Orogeny. Rationale for U-Pb analysis of rutile follows the success of a number of studies in high-grade metamorphic terranes including Ferreira-Filho (1994), Li *et al*. (2003) and Mezger *et al*. (1989). Subsequent U-Pb rutile age data is also likely to constrain timing of the retrograde evolution of the Petermann Orogeny (Cherniak 2000, Vry & Baker 2006).

Sample preparation

Rutile, titanite and zircon separation was performed at the University of Adelaide. Initially, a small piece of each sample was crushed using a jaw crusher. Sieving was performed using a combination of 425 and 75 μm mesh for a duration of several minutes for each sample. The 425-75 μm fraction was collected for subsequent refinement and the grains larger than 425 μm were crushed and sieved repeatedly until there was a sufficient fraction of 425-75 μm grains. Samples were further refined by conventional density methods to isolate heavier mineral components. Each heavy fraction was run through the Frantz to isolate the non-magnetic minerals of interest. Approximately 100 rutile and/or titanite and/or zircon grains of varying morphologies were hand-picked for each sample and mounted in epoxy resin along with the appropriate standards for each mount. The grains were then ground to approximately half their diameter to expose a representative section through the grain using a combination of polishing cloths.

Imaging of the mounts was undertaken at Adelaide Microscopy using a Phillips XL20 SEM with a Gatan CL detector. Titanite and rutile grains were observed with a backscattered electron detector and imaged, cathodluminescence (CL) imaging of zircons was necessary to investigate internal zonation. Prior to SHRIMP analysis the mounts were cleaned and then coated with 500 nm of high purity gold.

SHRIMP operating procedures and data reduction

U-Pb-Th analysis of rutile, titanite and zircon was conducted using the SHRIMP II (A) at the John De Laeter Centre for Mass Spectrometry at Curtin University, Perth. Titanite samples PE9 and DFC 507, rutile samples DFC 387, 441A and PE9, and zircon samples DFC 507 and 542 were analysed in separate sessions over the period 20^{th}-22^{nd} September, 2010. Detailed

operating procedures are outlined by Williams (1998). SHRIMP techniques relevant to titanite are described by Kinny (1997). For all analyses a beam diameter of 30 microns was used. Prior to each analysis, the spot was rastered with the beam for 2 minutes at 120 nA, to remove the gold coating and reduce surficial common lead and other sources of contamination. Six scans were run for each analysis spot and the results were averaged. The ^{204}Pb peak was resolved prior to analysis of each mount by analysing a sample of potassium feldspar from Olary, Broken Hill. U-Pb fractionation was corrected for by repeated analysis of a standard of a known age, the Khan standard was used to correct this for titanite analyses, WHQ for rutile, and BR266 and Temora for zircon. All data reduction was completed using KRILL software (Kinny 1997).

Titanite analyses from both samples showed low concentrations of ^{235}U (10-35 ppm) and consequently, low radiogenic components. Concentrations of common lead were detected for both titanite samples with the fraction of ^{204}Pb in ^{206}Pb ranging from 0.1-0.6. These values are significantly higher than can be attributed to other sources such as remnant gold-coating or contamination from the mount surface, which were estimated using the common Pb in the Khan standard (Kinny *et al.* 1994). Common lead corrections were therefore applied to all titanite analyses using KRILL. Extremely low precision is recorded for 207/206 Pb isotope ratios, reflecting the high concentrations of common lead.

Rutile analyses from all samples showed very low concentrations of ^{235}U (5-15 ppm) and consequently also had low radiogenic components. Throughout all rutile analyses there were negligible fractions of ^{204}Pb in ^{206}Pb ranging from 0.01-0.04 whereas ^{208}Pb counts were of the same magnitude as other isotopic Pb values. As thorium counts were consistently zero, ^{208}Pb values are assumed to be representative of the common lead composition in rutile samples analysed. Common lead corrections were applied to rutile analyses using KRILL. Corrected ^{208}Pb isotope values are quoted in Table 4, all errors are quoted at 1 sigma level.

LA-ICPMS operating procedures and data reduction

U-Th-Pb analysis of zircon was conducted using an Agilent 7500cs ICPMS coupled with a New Wave 213 nm Nd-YAG laser. Ablation was performed in a helium atmosphere, with a beam diameter of 30 μm, repetition rate of 5 Hz and laser intensity of 70%. Total acquisition time for each analysis was 110 seconds, and involved 40 seconds of background measurement, 10 seconds for beam and crystal stabilisation, and 60 seconds of sample ablation. Detailed operating conditions are outlined by Payne *et al*. (2006, 2007). U-Pb fractionation was corrected using the GEMOC GJ-1 standard (Jackson *et al.* 2004), and data reduction was completed using GLITTER software (Van Achterbergh. *et al.* 2001)Accuracy was also monitored by repeat analyses of the Czech internal zircon standard Plesovice (Sláma *et al.* 2008).

Quantified metamorphic analysis

Metamorphic phase diagrams were calculated based on bulk chemical compositions obtained in one of two ways. First, From rock powders analysed at Amdel Laboratories, Adelaide. Major elements were analysed by fusion of a 0.1 g sub-sample of the analytical pulp with lithium metaborate followed by dissolution in nitric acid solution to give a "total solution" for ICP-MS analysis. Analysis of trace and REE elements is achieved by digestion of up to 0.5 g of the analytical pulp in a HF/multi acid solution and introduced into an ICP-MS for the quantification of the elements of interest (Payne *et al.* 2010). Analysis via titration methods provides concentration of Fe^{2+}.

The second method of determining bulk compositions is based on measured mineral chemistry and mineral abundance. Mineral chemistry for samples was obtained via electron microprobe (EMP) analysis. Representative EMP analyses for each mineral in domain of the rock were used along with modal abundances, estimated from elemental maps (using imaging software package IMAGEJ), to estimate a bulk composition in an appropriate model chemical system. This technique was used because the distribution of metamorphically relevant minerals in several samples was particularly heterogeneous and/or confined to very localised and microscopic reaction domains. Where rocks are chemically and mineralogically heterogeneous, whole-rock analyses are not appropriate. The H_2O content was estimated based on assuming an amount of H2O in the hydrous minerals in the assemblage and is therefore controlled by the abundance of the hydrous phases.

Phase equilibria calculations

Metamorphic phase diagrams were calculated using THERMOCALC v3.33, using the internally consistent data set of Holland and Powell (1998; data set tcds55s, November 2003). Phase diagrams were calculated in geologically realistic systems NCFMASHTO (Na2O-CaO-FeO-MgO-Al2O3-SiO2-H2O-TiO2-Fe2O3) for sample PE9, and NCKFMASHTO (Na2O-CaO-FeO-MgO-Al2O3-SiO2-H2O-TiO2-Fe2O3) for sample 577C. These systems use *a-x* relationships of Diener *et al.* (2007) for amphiboles, Green, *et al.* (2007) for clinopyroxenes, White, *et al* (2007) for garnet, biotite and silicate melt, Holland & Powell. (2003) for K-feldspar and plagioclase, White *et al.* (2002) for magnetite and White *et al.* (2000) for ilmenite.

LA-ICPMS trace element analysis

Operating procedures and data reduction

Trace element analysis of titanite and zircon samples was performed at Adelaide microscopy using an Agilent 7500cs ICPMS equipped with a New Wave 213 nm Nd-YAG laser. Titanite analyses were conducted using a 50 µm beam diameter and 5 Hz repetition rate, and were performed overprinting existing SHRIMP pits of Pfitzner (2009). Zircon analyses were performed on rim domains using a 40 µm beam diameter, a repetition rate of 5 Hz and spots overprinted existing SHRIMP pits of Pfitzner (2009). Total acquisition time for each analysis was 110 seconds, and involved 40 seconds of background measurement, 10 seconds of beam stabilisation, and 60 seconds of ablation and collection. The NIST 610 standard was used for calibration, and accuracy of this standard was checked by measurements of the NIST 612 and NIST 614 glass standards. Data reduction was performed using GLITTER software (Van Achterbergh. *et al.* 2001). Internal calibration for titanite was completed using ^{30}Si obtained via electron microprobe analysis. Internal calibration for zircon analyses was conducted using a stoichiometric value for ^{30}Si in zircon.

Trace element thermometry

Temperatures estimated from trace element concentrations in this study employ the Zr-in-titanite thermometer of Hayden *et al*. (2008) and the Ti in zircon thermometer of Watson *et al*. (2006). These thermometers provide an independent estimate of temperature of titanite and zircon formation, where metamorphic phase diagram calculations are not performed. Therefore with this data it is possible to link the thermal conditions of accessory mineral growth with the U-Pb geochronology.

Thermometers for titanite and zircon are based on the limited exchange between the structural constituents of the two phases, namely, titanium and zirconium. Both thermometers are calibrated using trace element analysis completed on natural and synthetic examples of zircon and titanite. The thermometers are defined by a log-linear relationship between equilibrium Ti and Zr content (ppm by weight), pressure (GPa) and reciprocal absolute temperature (K):

$$\text{Log}\,(\text{Zr}_{\text{titanite}}) = 10.59 - \frac{7708}{T} - \frac{960P}{T} \qquad (1)$$

$$\text{Log}\,(\text{Ti}_{\text{zircon}}) = (6.01 \pm 0.03) - \frac{5080 \pm 30}{T} \qquad (2)$$

The incorporation of Zr into titanite is shown to be sensitive to pressure whereas the Ti in zircon thermometer is assumed to be independent of pressure. The Zr content of titanite is also not affected by the presence of either REE's or F-Al substitutions, implying that analytical error in determination of the Zr concentration provides the only uncertainties associated with temperature estimates (Watson *et al.* 2006, Hayden *et al.* 2008). Calculations using both the Zr in titanite and Ti in zircon thermometers require titanite and zircon must be in an equilibrium assemblage with both quartz and rutile.

Garnet diffusion-cooling modelling

The diffusion-cooling modelling code of Robl *et al.* (2007) was used to estimate cooling rates in order to constrain information about the retrograde evolution of the Petermann Orogeny. Garnets from sample Pe9 with a radius of 245 µm and and sample LH022b of radius 426.5

μm and 115.7 μm were modelled. All input parameters were constant except for the time interval which was varied in order to define a cooling profile. The value for *Xmg* of biotite = 0.58 was constant for all garnets in sample Pe9 as all analyses of Xmg = (Xmg/(Xmg+Xfe) of hornblende were between 0.57-0.59. Xmg of biotite was 0.69 for garnets a and b in sample LH022b. Diffusion coefficients applied are from Ganguly *et al.* (1998). User defined cooling histories were input based on geochronology and estimates on thermal conditions obtained in this study.

Results

Mineral chemistry

Group 1

Garnets from sample LH16B are dominantly almandine-grossular solid solution and exhibit subtle zoning, with X_{Fe} (Fe/Fe+Ca+Mg+Mn) varying from 0.63 at the cores to 0.60 at the rims, and X_{Ca} (Ca/Fe+Ca+Mg+Mn) ranging from 0.26 at the cores to 0.31 at the rims. X_{Mg} (Mg/Fe+Ca+Mg+Mn) is in the range 0.05-0.06. Spessartine is low, with X_{Mn} (Mn/Fe+Ca+Mg+Mn) in the range 0.03-0.05. Garnets from sample 577C are dominantly almandine-pyrope solid solution and exhibit very little zoning, with X_{Fe} only varying between 0.55 and 0.56 and X_{Mg} in the range 0.35-0.36. Spessartine is low, in the range 0.041-0.046. Garnet rims show enrichment relative to the cores with values of 0.048 compared to 0.02 at the core.

Biotite is uniformly titanium-rich across samples, with X_{Ti} (Ti/Ti+Fe+Al+Mg) ranging between 0.06-0.09. X_{Al} is uniformly high, with values generally in the range 0.29-0.3. X_{Mg} (Mg/Fe+Mg) values are also uniform across the group, in the range 0.38-0.42.

Hornblende in sample LH16B is highly calcic, with $Ca_{\boldsymbol{B}}$ ranging from 1.9-2, Na_B <0.5 and $(Ca+Na)_B$ values in the range 2.4-2.5. Samples plot within the pargasite-ferropargasite subgroup on a plot of X_{mg} (Mg/Mg+Fe^{2+}) (Leake *et al.* 1997).

Metamorphic plagioclase is highly sodic in all samples. In sample LH16B X_{ab} (Na/Na+Ca) is invariably between 0.87 and 0.9. In sample 577C X_{ab} ranges from 0.82 at the core to 0.67 at the rims. The albite content of K-feldspar is low in all samples, with X_{ab} (Na/Na+K) ranging from 0.09 to 0.16.

Group 2

Garnet is dominantly an almandine-grossular solid solution, X_{Fe} (Fe/Fe+Ca+Mg+Mn) in the range 0.5-0.6 and X_{Ca} (Ca/Fe+Ca+Mg+Mn) in the range 0.33-0.37. X_{Mg} (Mg/Fe+Ca+Mg+Mn) is in the range 0.035-0.045. Spessartine is low, with X_{Mn} (Mn/Fe+Ca+Mg+Mn) in the range 0.03-0.05.

Biotite is uniformly titanium-rich across samples, with X_{Ti} (Ti/Ti+Fe+Al+Mg) ranging between 0.06-0.07. X_{Al} is uniformly high, with values generally in the range 0.3-0.32. X_{Mg} (Mg/Fe+Mg) values are also uniform across the group, in the range 0.2-0.22.

Hornblende is uniformly calcic across the group, with $Ca_{\boldsymbol{B}}$ ranging from 1.75-1.85, Na_B <0.7 and $(Ca+Na)_B$ values in the range 2.4-2.5. Samples are magnesium-poor with X_{Mg} in the range 0.25-0.3.

Metamorphic plagioclase is highly sodic in all samples where X_{ab} (Na/Na+Ca) is invariably between 0.85 and 0.9. The albite content of K-feldspar is low in all samples, with X_{ab} (Na/Na+K) ranging from 0.09 to 0.12.

Clinopyroxene is classified within the Ca-Mg-Fe quadrilateral, having Ca+Ma+Fe^{2+} values ranging from 1.7-1.8 and Na varying between 0.08 and 0.19 (Morimoto 1988).

Clinopyroxene is uniformly calcic, with X_{Ca} (Ca/Fe^{2+}+Fe^{3+}Ca+Mg+Mn) values ranging from 0.4-0.43, and is contained within the diopside field. Group 2 samples are iron-rich, with X_{Mg} values in the range 0.38-0.4.

Group 3

X_{Fe} (Fe/Fe+Ca+Mg+Mn) of garnets in sample Pe9 varies between 0.51 at the core to 0.6 at the rims, X_{Ca} (Ca/Fe+Ca+Mg+Mn) is particularly uniform and ranges between 0.23 and 0.24. X_{Mg} (Mg/Fe+Ca+Mg+Mn) varies between 0.2 at the core to 0.13 at the rims. Spessartine is low, with X_{Mn} (Mn/Fe+Ca+Mg+Mn) in the range 0.03-0.031 (Fig. 4).

Biotite in sample Pe24 is uniformly titanium-rich across samples, with X_{Ti} (Ti/Ti+Fe+Al+Mg) ranging between 0.07-0.097. X_{Al} is high, with values generally in the range 0.39-0.42. X_{Mg} (Mg/Fe+Mg) values are in the range 0.01-0.021.

Hornblende is uniformly calcic across the group, with Ca_B ranging from 1.7-1.95, Na_B <0.7 and $(Ca+Na)_B$ values in the range 2.4-2.5. X_{Mg} is in the range 0.3-0.45.

Metamorphic plagioclase is highly sodic in all samples where X_{ab} (Na/Na+Ca) is invariably between 0.82 and 0.88. The albite content of K-feldspar in Pe24 is low in all samples, with X_{ab} (Na/Na+K) ranging from 0.08 to 0.10.

Calculated metamorphic phase equillbria

Pe9

Migmatitic sample Pe9 is located in the Cockburn Shear Zone (Fig. 2). This sample was chosen because U-Pb geochronology indicates deformation is Petermann aged (this study). The peak assemblage is garnet-clinopyroxene-hornblende-plagioclase-ilmenite-quartz-rutile

± H2O ± cz (see petrographic descriptions) and is constrained at *c.* 13-14 kbars and 700-750 ºC, based on the *P-T* psuedosection, Fig. 5. Garnet commonly has inclusions of plagioclase and clinozoisite which suggests that it grew at the expense of these minerals. This defines the dominant prograde reaction. The early retrograde path is defined by the breakdown of garnet and plagioclase to produce more hornblende, which is observed in the rock as hornblende coronae on garnet. The clinozoisite-bearing post-peak assemblage is defined by titanite coronae on rutile and occurs at T > *c.* 670ºC and P > *c.* 9 kbars. As these reactions are pressure dependent, it suggests that the apparent P-T path is steep although it is very unlikely that the path is anti-clockwise.

577C

Mylonitic sample 577C is located in the Mt. Charles Thrust in the eastern Mann Ranges (Fig. 2). This sample is conducive to metamorphic phase equilibria calculations because it contains kyanite and therefore must be of Petermann age as the Musgrave Orogeny had a geothermal gradient and temperatures too extreme for kyanite stability (Kelsey *et al.* 2009, Kelsey *et al.* 2010, Smithies *et al.* 2010). The peak assemblage is garnet-biotite-kyanite-quartz-K-feldspar-ilmenite-plagioclase-H_2O ± mus. Contouring for mineral composition constrains peak conditions at *c.* 11-13 kbars and 700-750ºC. Modal proportion of muscovite is < 1% and therefore it is feasible that the peak assemblage exists within the muscovite-bearing field. The minor proportion of muscovite in phase equilibria calculations may suggest that bulk composition is not entirely representative of the rock. Elemental mapping and mineral chemistry suggest that garnet was produced at the same time as plagioclase. Second generation of garnet growth is far more calcic than larger porphyroclastic garnets and plagioclase is zoned with increasing sodium at the rims (Figure 7). Compositional contours demonstrate the up-pressure increase of X_{Ca} in garnet and the decrease of X_{Ca} in plagioclase (Figure 6).

U-Pb-Th SHRIMP geochronology

Titanite age data

Diagrammatic representations of SHRIMP titanite age data for all samples are presented in Fig. 8, and analytical data are provided in Table 3. The spatial distribution of all samples is also shown in Fig. 2, along with their associated age estimates.

Sample Pe9

Twenty-eight analyses of an equivalent number of grains were conducted on sample PE9. One analysis is excluded from the final age estimates as it is are significantly discordant compared to the rest of the data due to appreciable concentrations of common lead. A linear regression through the ^{204}Pb corrected ^{206}Pb/^{238}U vs. ^{207}Pb/^{206}Pb isotope ratios produces a lower intercept age of 521±11 Ma with an MSWD of 1.7 when plotted on a Tera-Wasserburg concordia diagram (Fig. 8a).

Sample DFC507

Fifteen analyses were conducted on an equivalent number of titanite grains from sample DFC507. Five analyses are excluded from the final age estimates as they show appreciable concentrations of common lead. A linear regression through the ^{204}Pb corrected ^{206}Pb/^{238}U vs. ^{207}Pb/^{206}Pb isotope ratios produces a lower intercept age of 567±14 Ma with an MSWD of 0.46 when plotted on a Tera-Wasserburg concordia diagram (Fig. 8b).

Rutile age data

Diagrammatic representations of SHRIMP rutile age data for all samples are presented in Figures 9, and analytical data are provided in Table 4. The spatial distribution of all samples is also shown in Fig. 2, along with their associated age estimates.

Sample 441A

Fourteen analyses were conducted on an equivalent number of rutile grains from sample 441A. Seven analyses are excluded from the final age estimates as they show high concentrations of common lead. A weighted average of ^{208}Pb corrected ^{206}Pb/^{238}U ages yields an estimate of 490±18 Ma with an MSWD of 1.19 (Fig. 9a). A concordia plot of ^{208}Pb corrected ^{206}Pb/^{238}U vs. ^{207}Pb/^{235}U isotope ratios produces a concordia age of 496±18 Ma with an MSWD of 0.29 (Fig. 9b).

Sample DFC387

Fifteen analyses were conducted on an equivalent number of rutile grains from sample DFC 387. Five analyses are excluded from the final age estimates as they show appreciable amounts of common Pb. A weighted average of ^{208}Pb corrected ^{206}Pb/^{238}U ages yields an estimate of 502±31 Ma with an MSWD of 0.42 (Fig. 9c). A ^{208}Pb corrected ^{206}Pb/^{238}U vs. ^{207}Pb/^{235}U isotope ratio concordia plot produces a concordia age of 498±21 Ma with an MSWD of 0.26 (Fig. 9d).

Sample Pe9

Fifteen analyses were conducted on an equivalent number of rutile grains from sample PE9. One analyses is excluded from the final age estimates as they are significantly discordant compared to the rest of the data. A weighted average of ^{208}Pb corrected ^{206}Pb/^{238}U ages yields an estimate of 504±26 Ma with an MSWD of 3.4 (Fig. 9e).

Zircon age data

Diagrammatic representations of SHRIMP zircon age data for all samples are presented in Figure 10 , and analytical data are provided in Table 3. The spatial distribution of all samples is also shown in Fig. 2, along with their associated age estimates.

Sample DFC 507

Fourteen analyses were conducted on an equivalent number of zircon grains from sample DFC 507. A weighted average of ^{204}Pb corrected ^{207}Pb/^{206}Pb ages yields an age estimate of 1198±31 Ma with an MSWD of 1.7 (Fig. 10a).

S*ample 542*

Sixteen analyses were conducted on fourteen zircon grains from sample DFC 507. A weighted average of ^{204}Pb corrected ^{207}Pb/^{206}Pb ages yields an age estimate of 1099±29 Ma with an MSWD of 3.1 (Fig. 10b).

LA-ICPMS in-situ monazite age data

Forty analyses of twenty-three monazite grains were conducted on sample 577C, targeting both homogenous grains and grains that showed internal zoning, where both the darker cores and lighter rims were analysed. All age data is plotted on a conventional Concordia plot and presented as a probability density distribution. Despite the analysis of a wide variety of grain morphologies and variable internal features there are no systematic age brackets and there

appears to be only a single population of ages around *c.* 1200 Ma (Fig. 11). Several grains are concordant at *c.* 1200 Ma although the majority of the analyses are discordant. The analyses do not appear to define a linear trend that would reflect a single younger lead loss event. Some analyses appear to track toward infinite ^{207}Pb values that suggests the incorporation of common lead into crystal lattice (Fig. 11). A weighted average of the $^{207}Pb/^{206}Pb$ ages for analyses with >95% concordance produces an age estimate of 1214 ± 16 Ma, with an acceptable MSWD of 2.3, which is within error for the upper intercept estimate age (Fig. 11a). A concordia plot of the $^{207}Pb/^{206}Pb$ vs $^{238}U/^{206}Pb$ produces an upper intercept age estimate of 1210 ± 18 Ma with a high MSWD of 3.1 (Figure 11b). The upper intercept age is taken to be the accurate representation of the crystallisation age of monazite as it is defined by the few concordant analyses that reflect minimal Pb loss.

Trace element thermometry

Titanite temperature estimates

Titanite temperature estimates from sample PE24 are presented in Table 8. All titanite analyses correspond to Petermann-aged analyses, dated by Pfitzner (2009). A temperature estimate of 768 ± 15ºC is generated when calculated at a pressure of 10 kbars. The application of the Zr in titanite thermometer is based on a weighted average Zr content. The quoted error is largely based on the variation in Zr content and the associated temperature range. The pressure dependency of the thermometer causes uncertainty in the calculation, therefore errors are calculated at 1 GPa and allow for a pressure fluctuation of ±0.1 GPa, which yields an error of ±11 ºC. The 1 sigma detection error in the analysis generates an error of ±4 ºC.

Zircon temperature estimates

Zircon temperature estimates from samples PE24 are presented in Table 8. All zircon analyses correspond to Petermann-aged analyses, dated by Pfitzner (2009). The calculated value from recrystallised rims is 733.3 ± 23ºC. The application of the Ti in zircon thermometer is based on a weighted average Ti content. The quoted error is based on the variation in Ti content, which yields a temperature range. The 1 sigma errors are associated with a larger uncertainty of ±10ºC, as the overall titanium concentration is far lower relative to Zr in titanite. Uncertainties associated with calibration of the thermometer are included and contribute errors of ±13 ºC. Several analyses yielded concentrations that are an order of magnitude higher than the quoted average. The observed spectrometry signals for these analyses were variable and it was difficult to isolate a significant part of the signal that would result in data that is representative of a rim analysis and therefore these analyses were discounted from subsequent calculations. These extreme analyses were attributed to ablation through a thin recrystallised rim and subsequent analysis of the core, which may preserve a chemical signature reflecting a previous thermal event.

Garnet diffusion-cooling modelling

Pe9

An initial temperature of *c.* 760ºC followed by cooling at 5ºC/ My for 40 M.y. represents the cooling history required to replicate X_{Mg} zoning profiles observed in sample Pe9 (Fig. 12).

LH022B

Separate cooling histories were required to replicate zoning profiles observed in garnets from sample LH022B. The observed profile of the larger garnet is produced given a starting

temperature of 770ºC followed by cooling at 5ºC/ Ma for 5 M.y. (Fig. 13a). Reconstruction of the X_{Mg} profile of the small garnet requires a starting temperature of 770ºC followed by cooling at 4.8ºC/ Ma for 35 M.y. (Fig. 13c).

Discussion and Conclusions

There are two contrasting models regarding the duration of the Petermann Orogeny. Camacho *et al*. (2001, 2009) suggests that high-grade metamorphic rocks formed in the eastern part of the orogen (Davenport Shear Zone) by shear heating and that shear heating was causative in the overall metamorphism of the Petermann Orogeny. This implies that duration of metamorphism in any one part of the orogen is extremely short-lived (*c.* 1 My.) and that the crustal section of the lithosphere must have been comparatively refrigerated compared to regional geothermal gradients. Short-lived metamorphism is proposed based on garnet zoning profiles where calcium enrichment at the rims of garnet are interpreted to represent volume diffusion during peak thermal conditions and therefore represent an integrated duration of movement in a shear zone at peak temperatures. Camacho *et al.* (2009) also interprets the partial resetting of K-Ar systematics in relict K-feldspar to be indicative of a short-lived thermal event.

By contrast, Raimondo *et al*. (2009, 2010) suggests the Petermann Orogen is characterised by an intracontinental channel-flow system. As a result, deformation is pervasive, and in places, migmatitic in style. This style of deformation necessitates a hot, weak crust and implies that duration of metamorphism is far longer (*c.* 30 M.y.) and geothermal gradients are higher than suggested by Camacho *et al* (2009). Raimondo *et al.* (2009, 2010) proposes long-lived duration for the Petermann Orogeny based on geochronological constraints on the timing of

both the growth of zircon during peak metamorphism and the subsequent cooling of titanite through the closure of Pb diffusion.

It is improbable that the Petermann Orogeny synchronously involved both short-lived 'regional' and long-lived regional metamorphism. It is clear from previous studies that the Peterman Orogeny did not involve significant melting and is characterised by relatively low-geothermal gradient deep-crustal rocks, an observation that is seemingly at odds with conventional wisdom for collisional orogens. In the following, the data collected in this study is used to appraise and discuss the cold/short-lived vs long-lived hypotheses of Camacho *et al* (2009) and Raimondo *et al* (2009, 2010) respectively.

Age constraints on the metamorphic evolution

Titanite ages

Titanite grains commonly occur as corone around rutile and/or ilmenite, and occasionally almost entirely replacing these oxides. This suggests that titanite growth is a result of the retrogression of high-grade metamorphic rocks (Lucassen *et al.* 2010). This further suggests that the maximum age preserved by the titanite U-Pb system will be a record of post-peak metamorphism and thus will provide a minimum age constraint on peak metamorphic conditions. The textural relationship of titanite with respect to the peak metamorphic assemblage provides further evidence for titanite production due to retrograde reactions. Titanite occurs in the presence of rutile or ilmenite, garnet, clinozoisite, plagioclase, quartz and occasionally biotite and hornblende, this implies that titanite growth is controlled by reaction between these phases. The coronal habit of titanite around ilmenite or rutile suggests titanium is sourced from these oxides and less commonly from titanium-poor biotite. It is also

commonly in contact with garnet and plagioclase which suggests the breakdown of these minerals during decompression provides the source of Ca.

The timing of titanite growth will not necessarily be preserved by the U-Pb isotopic system, as a result of age estimates becoming decoupled from the timing of growth. If the closure temperature for the U-Pb system in titanite is below that of peak metamorphic conditions, then the possibility arises that age estimates will reflect timing of the closure of diffusion and not record the timing of growth *(*Frost *et al. 2001,* Cherniak 2006*).* Variation in closure temperature for minerals are due to grain size, crystal structure and internal dislocations as well as cooling rates (Pidgeon *et al.* 1996, Kelsey *et al.* 2003). Frost *et al*. (2001) and Cherniak & Watson (2001) estimate closure temperatures for titanite grains with a radius of 100 µm at a cooling rate of 10ºC/Ma, between 660ºC and 600ºC. Temperature estimates from this and previous studies on the Petermann Orogeny indicate that peak metamorphic conditions were elevated above the postulated closure temperatures, raising the possibility that U-Pb titanite ages correspond to the timing of cooling through Pb closure.

In the absence of zircon geochronology of Petermann age from the same samples from which titanite age data was collected in this study, it is not possible to unequivocally conclude whether the titanite U-Pb ages reflect growth or cooling ages. If the ages represent cooling ages then this places a minimum age on metamorphism. An intriguing aspect of the titanite U-Pb age data is the marked southward decrease in age from 567±14 Ma to 521±11 Ma. Raimondo *et al* (2009, 2010) also noted the same trend for samples further west in the Petermann orogen (effectively along strike). Raimondo *et al* (2009, 2010) equated differences in titanite age to differences in grain size, with the largest grains and oldest ages located more northerly, and the smaller titanite grains and younger ages located more southerly. As Raimondo was able to collect Petermann-aged zircon U-Pb data that had a similar age (identical within error) to the northerly titanite age data, those titanites were interpreted to be

recording growth ages. However, the correlation between decreasing titanite grain size to the south, and progressively younger ages in not observed in this study. This strongly suggests that the large differences in ages from north to south is not simply a function of grain size. Bulk compositional influences cannot readily be invoked (Kelsey *et al.* 2008) because there is not an observable decrease in titanite abundance southwards in the analysed samples.

Rutile ages

Rutile grains in all three samples analysed are interpreted to form part of the peak metamorphic assemblage. Similar to titanite, the closure temperatures for Pb diffusion in rutile will influence to interpretation of isotopic age data, and therefore the U-Pb signal systematics are not necessarily preserved and it follows that geochronology may not represent the timing of crystallisation, but rather the timing of closure of Pb diffusion (Cherniak 2000). Cherniak (2000) and Vry & Baker (2006) define the closure temperature of a 200 µm rutile grain with cooling rates of 1ºC/Ma, to be *c.* 600ºC. The closure temperature for U diffusion in rutile is considered to be strongly dependent on grain size, where a spread of ages may reflect different closure temperatures as a result of variations in diffusive volumes, rather than different events (Mezger *et al.* 1989, Cherniak 2000). Rutile grains from all samples analysed generally have diameters between 70 and 90 µm, therefore at estimated cooling rates of 3-5ºC/Ma, it would be expected that they would have slightly lower closure temperatures (*c.* 550-570ºC) and thus would result in lower age estimates.

Previous studies, and this study, estimate temperatures during the Petermann Orogeny that are greater than the expected closure temperature of most rutile grains (White & Clarke 1997, Scrimgeour & Close 1999, Vry & Baker 2006, Gregory *et al.* 2009, Raimondo *et al.* 2009). U-Pb age estimates on rutile are therefore likely to represent the timing of cooling through the closure temperature of Pb diffusion. In sample Pe9, titanite growth is petrographically

later than rutile, which implies that the minimum constraint on rutile crystallisation is 520 Ma, 20 M.y. earlier than rutile U-Pb age estimates of *c.* 500 Ma in all three analysed samples. Furthermore, the uniformity of the ages and the spatial proximity of the samples suggests that all rutile age estimates in this study are reflective of cooling through the closure temperature of Pb diffusion.

U-Pb geochronology from this and other studies suggest that the recorded thermal regime in the Petermann Orogeny was long-lived. The earliest constraints on peak metamorphic conditions in the west Musgrave Province are recorded by dating of zircon and titanite which yields U-Pb ages of at *c.* 575 Ma (Raimondo *et al.* 2010). In the western Mann Ranges zircon ages constrain 'peak' metamorphism at *c.* 560 Ma (Scrimgeour & Close 1999). In the Cockburn Shear Zone (CSZ) Gregory *et al*. (2009) report U-Pb allanite and zircon ages of *c.* 559 Ma, corresponding to peak metamorphic conditions and partial melting. Zircon and titanite ages similarly constrain peak metamorphism at *c.* 540 Ma (Pfitzner 2009). A titanite age of *c. 5*20 Ma, from the CSZ collected in this study, interpreted to represent the timing of Pb closure through temperatures of approximately 650°C, suggests that the orogen has cooled by > 100ºC from peak conditions due to exhumation from 12-14 to 6-7 kbars (Fig. 5). If peak metamorphism is conservatively constrained to between 575 and 540 Ma, the duration of high-T metamorphic conditions during the Petermann orogeny is at least 35 M.y. At face value, this outcome seems more consistent with the findings and interpretations of Raimondo *et al.* (2009, 2010) rather than Camacho *et al.* (2009).

Thermobarometric evolution and exhumation history

The case for rapid, short-lived orogenesis advocated by Camacho *et al.* (2001, 2009) is based largely on cooling rates estimated from elemental zonation profiles preserved in garnet from a mylonite. The study of Camacho *et al.* (2009) is based upon the diffusion rate and thermal implications of the internal zoning in a garnet. During the course of this study, garnets of varying sizes were routinely analysed by electron microprobe to monitor the chemistry and any elemental zonation that may be preserved. Larger garnet grains (radius ~500-700 μm) consistently preserve diffusional profiles that are different to smaller garnet grains (radius ~50-100 μm) (Figure 13). The consistent observed difference in diffusion profile can be explained as the larger one has been broken and pulverised during mylonitisation. Conversely, the smaller garnet grain is likely not been broken during mylonitisation, as it may have been small enough to be transported in the mylonitic flow. The result of this is that the 'new' rim of a broken garnet grain would develop a new diffusion profile that would record a shorter duration of the thermal history compared to a grain that has not been broken. Results of garnet-diffusion modelling by Camacho *et al*. (2009) is based on very large garnet grains (radius ~ 1000 μm) from a highly mylonitised rock. It is therefore highly likely that garnet grains analysed have been broken and subsequently new diffusion profiles have developed, in which case analysis of narrowly zoned rims may lead to a misleading interpretation that the thermal regime during the Petermann Orogeny was short-lived.

Zoning in garnet samples is interpreted to be a result of Fe-Mg exchange between garnet and biotite or hornblende. A decrease in temperature in a equilibrium system containing garnet and biotite will cause the exchange of iron and magnesium where garnet will become enriched in iron and biotite will become more enriched in magnesium. Therefore, in

principle, the diffusion of Fe-Mg in a garnet-biotite system should represent a record of the cooling history of the mineral assemblage.

Fe-Mg diffusivity in garnet is strongly dependent on temperature such that the rate of exchange will decrease with decreasing temperatures and consequently, the diffusive volume of the garnet will decrease. This implies that in a cooling system, the outer rim of a garnet will undergo significantly more diffusion than the core. The diffusion-modelling code of Robl *et al.* (2007) allows an estimation of the cooling rates based on garnet zoning profiles that are a result of Fe-Mg exchange with biotite. Diffusion modelling was performed with the aim to constrain rates of cooling in order to provide information about the retrograde evolution of the Petermann Orogeny.

Garnets from samples Pe9 and LH022b are considered to be suitable for diffusion-cooling modelling as they adequately satisfy the conditions outlined by Robl *et al.* (2007). The calculation of the X_{Mg} across a garnet grain outlined is dependent on X_{Fe}, X_{Mg}, molar weight, mass density and volume of biotite. These parameters are non-unique to biotite and therefore altering these parameters to suitably model garnet-hornblende exchange is feasible. Internal zoning profiles show that garnets exhibit relatively flat cores and rims that are increasingly Fe-rich and Mg-poor (figure 4c). There is minor zoning of calcium in sample Pe9, where garnet rims are Ca-poor compared to cores, however this is considered to have minimal impact on the Fe-Mg ratio.

Garnets from sample LH022b preserve X_{Mg} values that decrease from core to rim (Figure 13 (a) and (b). Comparison of the modelled profiles shows that the two garnet grains record a different duration of the thermal history This difference is interpreted to be a result of varying grain size, where the larger garnet (r= 426.5 um) preserves a shorter duration of 5 Myr compared to the smaller garnet (r= 115.7 um) which preserves a duration of 35 Myr. The

difference can be explained as the larger one has been broken and pulverised during mylonitisation. The 'new' rim of the broken garnet grain would develop a diffusion profile that would record a shorter and duration of the thermal history and would lead to erroneous interpretation. Conversely, the smaller garnet grain is likely not been broken during mylonitisation, as it may have been small enough to be transported in the mylonitic flow, thus preserving a diffusion profile that records the entire duration of the thermal history. Therefore the minimum duration of cooling during the Petermann Orogeny was recorded by the smaller garnet grain and can be constrained to 35 Myr.

Subsequent average cooling rates experienced after peak metamorphic conditions can be constrained by the timing of growth of peak metamorphic accessory minerals and the timing of cooling through the closure temperature (Gregory *et al.* 2009, Raimondo *et al.* 2009, 2010). Cooling rates in the western Mann ranges can be estimated using U-Pb geochronology and constraints on the physical conditions from the Cockburn Shear Zone. Peak temperatures estimated in this study of *c.* 750ºC are recorded by Ti-in-zircon thermometry at *c.* 540 Ma. If the ages determined from titanite grains corresponds to cooling below the closure of Pb diffusion then an estimate of *c.* 600-650ºC can be placed at *c.* 520 Ma. Similarly, if rutile ages correspond to closure of Pb diffusion then an additional estimate of approximately 550-600ºC can be placed at *c.* 500 Ma. This implies a temperature decrease of 150-200ºC over a period of 40 M.y. at an average rate of 3.75-5ºC/Ma. This is consistent with garnet diffusion-cooling modelling, which estimate cooling rates of 5ºC/My in the western Mann ranges and 5.6ºC/My from the eastern Mann Ranges. These are comparable to findings of Raimondo *et al.* (2009, 2010) who estimates cooling of ~1.8-5.8ºC/My in the Bates Region (Figure 2), and Hallet (2007) who estimates cooling rates of *c.* 5ºC/My in the Angatja Region (Figure 2).

Exhumation rates in the western Musgrave ranges can be estimated by using the calculated *P-T* equilibria, geochronology and cooling rate estimates. Integrated geochronology and

calculated phase diagrams indicate that cooling from peak conditions of metamorphism of *c.* 14 kbars and 750°C (this study) at *c.* 540 Ma (Pfitzner 2009) to conditions of *c.* 7 kbars and 550°C at *c.* 500 Ma (this study). The rate of exhumation is therefore *c 7* kbars (*c.* 20 km**)** in 40 M.y., which equates to ~500 m/Ma or 0.5 mm/yr. Cooling rates of 5ºC/Ma and physical conditions of 12-14 kbars recorded in the eastern Mann Ranges are consistent with estimates of 34-5ºC/Ma further to the west and therefore it is likely that exhumation rates are comparable despite the lack of constraints on the timing of orogenesis in the eastern Mann Ranges. These findings also suggest that final exhumation had not occurred by *c.* 500 Ma and that *P-T* conditions in the Musgrave Province were at least 6 kbars and 550ºC at this time. This implies that the Musgrave Province was still buried relatively deeply at 500 Ma. Exhumation rates and cooling rates are however, consistent with the exhumation history of the Petermann Orogeny being dominantly controlled by slow average convergence rates of <2 mm/yr (Camacho *et al.* 1997, Sandiford *et al.* 2001). This may suggest that plate margin was ultimately responsible for driving intraplate orogenesis (Aitken & Betts 2009a).

Thermal state of the crust

Estimates of peak metamorphic conditions during the Petermann Orogeny in the Western Mann Ranges from calculated metamorphic phase diagrams and thermometry suggest apparent geothermal gradients of *c.* 20ºC/km, assuming a pressure gradient of 0.3 kbars per kilometre. Estimates are consistent with gradients calculated by Raimondo *et al*. (2010) and Scrimgeour & Close (1999) obtained from the core of the Petermann orogen. The deeply exhumed rocks of the core of the orogen preserve shallow gradients comparable to average stable cratonic geothermal gradients, implying that the crust was not significantly thermally perturbed during the Petermann Orogeny (Lambert 1983).

That the long-lived Petermann Orogeny preserves a relatively cold thermal regime is an unresolved issue. That the crust can remain “cold” while “experiencing” long-lived tectonism could reflect one or more of several things : 1) the rocks are particularly poor conductors of heat i.e. the thermal time constant of the lithosphere was even greater than the duration of tectonism; 2) the crust was depleted in heat producing elements ; 3) the Centralian Superbasin overlying the Musgrave Province prior to the Petermann Orogeny was thick but contained an abundance of poorly insulating sediments. Whatever the reason, this raises the additional question of how did the crust deform in apparently ‘cold’ crust?

Results of this study indicate that the physical conditions of metamorphism (12-14 kbars and 700-750ºC), slow cooling rates (3.75-5.6 ºC/My), slow exhumation rates (0.5 mm/yr) and the subsequent timing and duration of orogenesis associated with the Petermann Orogeny are comparable between regions of pervasive deformation and associated localised migmitisation to the west, and areas of discrete mylonitisation to the east. Therefore the variation in the style of structural reworking along the Petermann Orogen from discrete and apparently cold, to migmatitic and pervasive and apparently hot, does not appear to reflect variations in the thermal regime across the orogen. This implies that there must another parameter controlling the style of deformation within the Petermann Orogeny. It is possible that this is a reflection of variation in the partioning of fluids which control the deformational response of the crust.

This study has integrated transferable and generally applicable methodologies to provide further understanding of the pressure-temperature-time evolution of the Petermann Orogeny. The study lends support to the notion that the Petermann Orogeny was a long-lived event, consisted of a long-lived thermal event of minimum 45 Ma duration and involved slow, exhumation-driven cooling. This study does not support the notion that orogenesis was extremely short-lived and does not advocate the theory that shear heating was the driver for metamorphism during the Petermann Orogeny. Now that long-lived intraplate orogenesis

seems to be established, this study provides a platform for the investigation of why and how such relatively cool thermal regimes were sustained for such a prolonged amount of time, and why orogenesis was focused in an apparently cold region of the crust/lithosphere.

Acknowledgements

Thanks are due to my supervisors David Kelsey and Martin Hand, for their assistance and constant stimulation of my passion for screwed up rocks. Thanks must go to all who collected the huge suite of samples and data at my disposal. Thanks to Ben Wade and Angus Netting at Adelaide Microscopy for their technical support during the vast time spent down there, as well as Kathryn Cutts for her help on the laser. Particular thanks to Justin Payne who was always willing to lend a hand with any procedure or interpretation of data you can think of. Big thanks to Rich Taylor and Chris Clark at Curtin University for their assistance on the SHRIMP and overall with U-Pb dating. Thanks also to the Geological Society of Australia for providing the opportunity to attend the AESC this year . Cheers to the Honours class of 2010, in particular, Buchs for the round at 4, Knighty for his amazing illustrator skills and never-ending peanut supply, Brianna for our insightful “Petermann” conferences, and the F1 lads. Last but not least, thanks to Mum & Dad, Deb, Jules, Danny and my entire family for keeping everthing in perspective and their endless support. Special thanks to Amy for all the dinners at uni, late nights and lots of smiles.

References

AITKEN A. R. A. & BETTS P. G. 2009a. Constraints on the Proterozoic supercontinent cycle from the structural evolution of the south-central Musgrave Province, central Australia. *Precambrian Research* **168**, 284-300.

AITKEN A. R. A. & BETTS P. G. 2009b. Multi-scale integrated structural and aeromagnetic analysis to guide tectonic models: An example from the eastern Musgrave Province, Central Australia. *Tectonophysics* **476**, 418-435.

AITKEN A. R. A., BETTS P. G. & AILLERES L. 2009. The architecture, kinematics, and lithospheric processes of a compressional intraplate orogen occurring under Gondwana assembly: The Petermann orogeny, central Australia. *Lithosphere* **1**, 343-357.

CAMACHO A., COMPSTON W., MCCULLOCH M. & MCDOUGALL I. 1997. Timing and exhumation of eclogite facies shear zones, Musgrave Block, central Australia. *Journal of Metamorphic Geology* **15**, 735-751.

CAMACHO A. & FANNING C. M. 1995. Some isotopic constraints on the evolution of the granulite and upper amphibolite facies terranes in the eastern Musgrave Block, central Australia. *Precambrian Research* **71**, 155-181.

CAMACHO A., MCDOUGALL I., ARMSTRONG R. & BRAUN J. 2001. Evidence for shear heating, Musgrave Block, central Australia. *Journal of Structural Geology* **23**, 1007-1013.

CAMACHO A., YANG P. & FREDERIKSEN A. 2009. Constraints from diffusion profiles on the duration of high-strain deformation in thickened crust. *Geology* **37**, 755-758.

CHERNIAK D. 2006. Zr diffusion in titanite. *Contributions to Mineralogy and Petrology* **152**, 639-647.

CHERNIAK D. J. 2000. Pb diffusion in rutile. *Contributions to Mineralogy and Petrology* **139**, 198-207.

DIENER J. F. A., POWELL R., WHITE R. W. & HOLLAND T. J. B. 2007. A new thermodynamic model for clino- and orthoamphiboles in the system Na2O–CaO–FeO–MgO–Al2O3–SiO2–H2O–O. *Journal of Metamorphic Geology* **25**, 631-656.

EDGOOSE C. J., I. R. SCRIMGEOUR, AND D. F. CLOSE 2004. Geology of the Musgrave Block, Northern Territory, Report 15, 44p. *Northern Territory Geological Survey*.

ELLIS D. J. & MABOKO M. A. H. 1992. Precambrian tectonics and the physicochemical evolution of the continental crust. I. The gabbro-eclogite transition revisited. *Precambrian Research* **55**, 491-506.

EVINS P. M., SMITHIES R. H., HOWARD H. M., KIRKLAND C. L., WINGATE M. T. D. & BODORKOS S. 2010. Devil in the detail; The 1150-1000 Ma magmatic and structural evolution of the Ngaanyatjarra Rift, west Musgrave Province, Central Australia. *Precambrian Research* **183, 572-588**.

FERREIRA-FILHO C. F., KAMO S. L., FUCK R. A., KROGH T. E. & NALDRETT A. J. 1994. Zircon and rutile U-Pb geochronology of the Niquelândia layered mafic and ultramafic intrusion, Brazil: constraints for the timing of magmatism and high grade metamorphism. *Precambrian Research* **68**, 241-255.

FLÖTTMANN T., HAND M., CLOSE D., EDGOOSE C. & SCRIMGEOUR I. R. 2004. Thrust tectonic styles of the intracratonic Alice Springs and Petermann Orogenies, central Australia. *in Thrust tectonics and hydrocarbon systems., edited by K. McClay, pp. 538-557, American Association of Petroleum Geologists Memoir.*

FROST B. R., CHAMBERLAIN K. R. & SCHUMACHER J. C. 2001. Sphene (titanite): phase relations and role as a geochronometer. *Chemical Geology* **172**, 131-148.

GANGULY J., CHENG W. & CHAKRABORTY S. 1998. Cation diffusion in aluminosilicate garnets: experimental determination in pyrope-almandine diffusion couples. *Contributions to Mineralogy and Petrology* **131**, 171-180.

GLIKSON A. Y., A. J. STEWART, C. G. BALLHAUS, G. L. CLARKE, E. H. J. FEEKEN, J. H. LEVEN, J. W. SHERATON, AND S. S. SUN 1996. Geology of the western Musgrave Block, central Australia, with particular reference to the mafic-ultramafic Giles Complex. *GSO Bulletin* **239**.

GLIKSON A. Y., C. G. BALLHAUS, G. L. CLARKE, J. W. SHERATON, A. J. STEWART, AND S. S. SUN 1995. Geological framework and crustal evolution of the Giles mafic–ultramafic complex and environs, western Musgrave Block, central Australia. *AGSO Journal of Australian Geology and Geophysics*, 41-67.

GREEN E., HOLLAND T. & POWELL R. 2007. An order-disorder model for omphacitic pyroxenes in the system jadeite-diopside-hedenbergite-acmite, with applications to eclogitic rocks. *American Mineralogist* **92**, 1181-1189.

GREGORY C. J., BUICK I. S., HERMANN J. & RUBATTO D. 2009. Mineral-scale Trace Element and U-Th-Pb Age Constraints on Metamorphism and Melting during the Petermann Orogeny (Central Australia). *J. Petrology*, egn077.

HALLET L. 2007. Pressure-temperture conditions and kinematic framework of the Petermann Orogeny in the central Musgrave Province. *University of Adelaide Honours Thesis (unpubl.).*

.

HAND M. & SANDIFORD M. 1999. Intraplate deformation in central Australia, the link between subsidence and fault reactivation. *Tectonophysics* **305**, 121-140.

HAYDEN L. A., WATSON E. B. & WARK D. A. 2008. A thermobarometer for sphene (titanite). *Contributions to Mineralogy & Petrology* **155**, 529-540.

HOLLAND T. & POWELL R. 2003. Activity–composition relations for phases in petrological calculations: an asymmetric multicomponent formulation. *Contributions to Mineralogy and Petrology* **145**, 492-501.

HOLLAND T. J. B. & POWELL R. 1998. An internally consistent thermodynamic data set for phases of petrological interest. *Journal of Metamorphic Geology* **16**, 309-343.

JACKSON S. E., PEARSON N. J., GRIFFIN W. L. & BELOUSOVA E. A. 2004. The application of laser ablation-inductively coupled plasma-mass spectrometry to in situ U-Pb zircon geochronology. *Chemical Geology* **211**, 47-69.

KELSEY D., POWELL R., WILSON C. & STEELE D. 2003. (Th+U)-Pb monazite ages from Al-Mg-rich metapelites, Rauer Group, east Antarctica. *Contributions to Mineralogy and Petrology* **146**, 326-340.

KELSEY D. E., CLARK C. & HAND M. 2008. Thermobarometric modelling of zircon and monazite growth in melt-bearing systems: examples using model metapelitic and metapsammitic granulites. *Journal of Metamorphic Geology* **26**, 199-212.

KELSEY D. E., HAND M., SMITHIES H., EVINS P., CLARK C. & KIRKLAND C. 2009. High-temperature, high geothermal gradient metamorphism in the Musgrave Province, central Australia; potential constraints on tectonic setting. In: Timms, N.E., Foden, J., Evans, K.E. & Clark, C. (eds). *Kangaroo Island 2009, Biennial Conference of the Specialist Group for Geochemistry, Mineralogy and Petrology, November 2009, Geological Society of Australia Abstracts No. 96, p. 28.*

KELSEY D. E., SMITHIES R. H., HAND M., EVINS P. M., CLARK C. & KIRKLAND C. 2010. What is the tectonic setting of long-lived Grenvillian-aged ultrahigh temperature, high geothermal gradient metamorphism in the Musgrave Province, central Australia? Geological Society of America Abstracts with Programs, 42(5), Denver, Colorado, Oct-Nov 2010.

.

KINNY P. D. 1997. Users guide to U-Th-Pb dating of titanite, perovskite, monazite and baddeleyite using the W.A. SHRIMP. W.A. Isotope Science Research Centre Report no. SPS 693/1997/AP72, Curtin University of Technology, Perth, 21pp.

KINNY P. D., MCNAUGHTON N. J., FANNING C. M. & MAAS R. 1994. 518 Ma sphene (titanite) from the Khanpegmatite, Namibia, southwest Africa: A potential ion-microprobe standard. In: Eighth International Conference on Geochronology, Cosmochronology and Isotope Geology Abstracts. . *US Geological Survey Circular 1107, Berkeley, 171*.

KORSCH R. J., GOLEBY B. R., LEVEN J. H. & DRUMMOND B. J. 1998. Crustal architecture of central Australia based on deep seismic reflection profiling. *Tectonophysics* **288**, 57-69.

LAMBECK K. & BURGESS G. 1992. Deep crustal structure of the Musgrave Block, central Australia: Results from teleseismic travel-time anomalies. *Australian Journal of Earth Sciences: An International Geoscience Journal of the Geological Society of Australia* **39**, 1 - 19.

LAMBERT R. S. J. 1983. Metamorphism and thermal gradients in the Proterozoic continental crust. *Geological Society of America* **Memoir**, 155-165.

LEAKE B., WOOLLEY A. R., ARPS C. E. S., BIRCH W. D., GILBERT M. C., GRICE J. D., HAWTHORNE F. C., KATO A. K., KISCH H. J., KRIVOVICHEV V. G., LINTHOUT K., LAIRD J., MANDARINO J. A., MARESCH W. V., NICKEL E. H., ROCK N. M. S., SCHUMACHER J. C., SMITH D. C., STEPHENSON N. C. N., UNGARETTI L., WHITTAKER E. J. W. & YOUZHI G. 1997. Nomenclature of amphiboles: Report of the Subcommittee on Amphiboles of the International Mineralogical Association, Commission on New Minerals and Mineral Names. *The Canadian Mineralogist* **35**.

LI Q., LI S., ZHENG Y.-F., LI H., MASSONNE H. J. & WANG Q. 2003. A high precision U-Pb age of metamorphic rutile in coesite-bearing eclogite from the Dabie Mountains in central China: a new constraint on the cooling history. *Chemical Geology* **200**, 255-265.

LINDSAY J. F., KORSCH R. J. & WILFORD J. R. 1987. Timing the breakup of a Proterozoic supercontinent: Evidence from Australian intracratonic basins. *Geology* **15**, 1061-1064.

LINDSAY J. F. & LEVEN J. H. 1996. Evolution of a Neoproterozoic to Palaeozoic intracratonic setting, Officer Basin, South Australia. *Basin Research* **8**, 403-424.

LUCASSEN F., DULSKI P., ABART R., FRANZ G., RHEDE D. & ROMER R. 2010. Redistribution of HFSE elements during rutile replacement by titanite. *Contributions to Mineralogy and Petrology* **160**, 279-295.

MABOKO M. A. H., MCDOUGALL I., ZEITLER P. K. & WILLIAMS I. S. 1992. Geochronological evidence for ~ 530–550 Ma juxtaposition of two Proterozoic metamorphic terranes in the Musgrave Ranges, Central Australia. *Australian Journal of Earth Sciences: An International Geoscience Journal of the Geological Society of Australia* **39**, 457 - 471.

MEZGER K., HANSON G. N. & BOHLEN S. R. 1989. High-precision UPb ages of metamorphic rutile: application to the cooling history of high-grade terranes. *Earth and Planetary Science Letters* **96**, 106-118.

MORIMOTO N. 1988. Nomenclature of Pyroxenes. *Mineralogy and Petrology* **39**, 55-76.

PAYNE J. L., FERRIS G., BAROVICH K. M. & HAND M. 2010. Pitfalls of classifying ancient magmatic suites with tectonic discrimination diagrams: An example from the Paleoproterozoic Tunkillia Suite, southern Australia. *Precambrian Research* **177**, 227-240.

PFITZNER H. 2009. The metamorphic evolution of the Petermann Orogen, Musgrave Province, central Australia: Constraining P-T-t and cooling rates in high grade rocks. *University of Adelaide Honours Thesis (unpubl.)*.

PIDGEON R. T., BOSCH D. & BRUGUIER O. 1996. Inherited zircon and titanite U---Pb systems in an Archaean syenite from southwestern Australia: implications for U---Pb stability of titanite. *Earth and Planetary Science Letters* **141**, 187-198.

PYSKLYWEC R. N. & BEAUMONT C. 2004. Intraplate tectonics: feedback between radioactive thermal weakening and crustal deformation driven by mantle lithosphere instabilities. *Earth and Planetary Science Letters* **221**, 275-292.

RAIMONDO T., COLLINS A. S., HAND M., WALKER-HALLAM A., SMITHIES R. H., EVINS P. M. & HOWARD H. M. 2009. Ediacaran intracontinental channel flow. *Geology* **37**, 291-294.

RAIMONDO T., COLLINS A. S., HAND M., WALKER-HALLAM A., SMITHIES R. H., EVINS P. M. & HOWARD H. M. 2010. The anatomy of a deep intracontinental orogen. *Tectonics* **29**, TC4024.

ROBL J., HERGARTEN S., STÜWE K. & HAUZENBERGER C. 2007. THERMAL HISTORY: A new software to interpret diffusive zoning profiles in garnet. *Computers & Geosciences* **33**, 760-772.

SANDIFORD M. & HAND M. 1998. Controls on the locus of intraplate deformation in central Australia. *Earth and Planetary Science Letters* **162**, 97-110.

SANDIFORD M., HAND M. & MCLAREN S. 2001. Tectonic feedback, intraplate orogeny and the geochemical structure of the crust: a central Australian perspective. *Geol. Soc. Spec. Publ.* **184(1), 195–218, doi:10.1144/GSL.SP.2001. 184.01.10.**

SCRIMGEOUR I. R. & CLOSE D. F. 1999. Regional high-pressure metamorphism during intracratonic deformation: the Petermann Orogeny, central Australia. *Journal of Metamorphic Geology* **17**, 557-572.

SLÁMA J., KOSLER J., CONDON D. J., CROWLEY J. L., GERDES A., HANCHAR J. M., HORSTWOOD M. S. A., MORRIS G. A., NASDALA L., NORBERG N., SCHALTEGGER U., SCHOENE B., TUBRETT M. N. & WHITEHOUSE M. J. 2008. Plesovice zircon -- A new natural reference material for U-Pb and Hf isotopic microanalysis. *Chemical Geology* **249**, 1-35.

SMITHIES R., HOWARD H., EVINS P., KIRKLAND C., KELSEY D., WINGATE M. H. M., COLLINS A., BELOUSOVA E. & ALLCHURCH S. 2010. Geochemistry, geochronology, and petrogenesis of Mesoproterozoic felsic rocks in the west Musgrave Province, Central Australia, and implications for the Mesoproterozoic tectonic evolution of the region. *Geological Survey of Western Australia* **Report 106**.

SUN S. S., C. M. GRAY, J. W. SHERATON, AND A. Y. GLIKSON 1996. Zircon U–Pb chronology and neodymium isotopic study of tectonothermal and crust-forming events in the Tomkinson Ranges, western Musgrave Block, Western Australia. *AGSO Journal of Australian Geology and Geophysics*, 14-16.

VAN ACHTERBERGH. E., RYAN C. G., JACKSON S. E. & GRIFFIN W. L. 2001. Data reduction software for LA-ICPMS. In: Laser-ablation-ICPMS in the earth sciences; principles and applications. *Mineralogical Association of Canada, Ottowa, ON, Canada*.

VRY J. K. & BAKER J. A. 2006. LA-MC-ICPMS Pb-Pb dating of rutile from slowly cooled granulites: Confirmation of the high closure temperature for Pb diffusion in rutile. *Geochimica et Cosmochimica Acta* **70**, 1807-1820.

WADE B. P., HAND M. & BAROVICH K. M. 2005. Nd isotopic and geochemical constraints on provenance of sedimentary rocks in the eastern Officer Basin, Australia: implications for the duration of the intracratonic Petermann Orogeny. *Journal of the Geological Society* **162**, 513-530.

WADE B. P., KELSEY D. E., HAND M. & BAROVICH K. M. 2008. The Musgrave Province: Stitching north, west and south Australia. *Precambrian Research* **166**, 370-386.

WALTER M. R., VEEVERS J. J., CALVER C. R. & GREY K. 1995. Neoproterozoic stratigraphy of the Centralian Superbasin, Australia. *Precambrian Research* **73**, 173-195.

WATSON E., WARK D. & THOMAS J. 2006. Crystallization thermometers for zircon and rutile. *Contributions to Mineralogy and Petrology* **151**, 413-433.

WHITE, CLARKE & NELSON 1999. SHRIMP U–Pb zircon dating of Grenville-age events in the western part of the Musgrave Block, central Australia. *Journal of Metamorphic Geology* **17**, 465-481.

WHITE, POWELL, HOLLAND & WORLEY 2000. The effect of TiO2 and Fe2O3 on metapelitic assemblages at greenschist and amphibolite facies conditions: mineral equilibria calculations in the system K2O–FeO–MgO–Al2O3–SiO2–H2O–TiO2–Fe2O3. *Journal of Metamorphic Geology* **18**, 497-511.

WHITE R. W. & CLARKE G. L. 1997. The Role of Deformation in Aiding Recrystallization: an Example from a High-pressure Shear Zone, Central Australia. *J. Petrology* **38**, 1307-1329.

WHITE R. W., POWELL R. & CLARKE G. L. 2002. The interpretation of reaction textures in Fe-rich metapelitic granulites of the Musgrave Block, central Australia: constraints from mineral equilibria calculations in the system K2O–FeO–MgO–Al2O3–SiO2–H2O–TiO2–Fe2O3. *Journal of Metamorphic Geology* **20**, 41-55.

WHITE R. W., POWELL R. & HOLLAND T. J. B. 2007. Progress relating to calculation of partial melting equilibria for metapelites. *Journal of Metamorphic Geology* **25**, 511-527.

WILLIAMS I. S. 1998. U-Th-Pb Geochronology by Ion Microprobe. In: Applications of microanalytical techniques to understanding mineralising processes (edited by McKibben, M. A., Shanks III, W. C. & Ridley, W. I.) Reviews in Economic Geology 7, 1-35.

ZHAO J.-X., MCCULLOCH M. T. & KORSCH R. J. 1994. Characterisation of a plume-related ~ 800 Ma magmatic event and its implications for basin formation in central-southern Australia. *Earth and Planetary Science Letters* **121**, 349-367.

Figure captions

Figure 1- a) Regional geology map of the Musgrave Province showing its position relative to the intraplate Amadeus and Officer Basin. East-west trending Petermann structures are highlighted. Modified from Glikson et al. (1995). Red boxes highlight area of study (refer to Figure 2).

Figure 2- Simplified geology of the Western Musgrave Province, highlighting the high-grade metamorphic rocks between the Mann Fault and the Woodroofe Thrust and the locations of geochronology outlined in Table 1, thermobarometric and cooling rate estimates. *P-T* estimates in the eastern Mann Ranges are sourced from Hallet. (2007). Map is adapted from the Mann and Hanging Knoll 1:250000 map sheets, the Bates 1:100000 map sheet and the Petermann Ranges 1:500000 map sheet. Inset map shows intracratonic basins and major tectonic elements of central and western Australia; AB, Arunta Block; AMB, Amadeus Basin; GB, Georgina Basin; MB, Musgrave Block; NB, Ngalia Basin; OB, Officer Basin. Modified from Camacho and McDougall [2000] and Raimondo et al. (2010).

Figure 3- Photomicrographs of petrographic relationships. Width of view is 2.5 mm unless indicated

a) *Sample LH016.* Gneissic layer of K-feldspar, quartz and plagioclase surrounding a layer of hornblende aggregates and poikiloblastic garnet. b) *Sample LH114*. Metamorphic biotite occurring in contact with porphyroblastic garnet that is surrounded by a foliated matrix of quartz, biotite, plagioclase and clinozoisite. Porphyroblastic K-feldspar is also wrapped by the same foliation. Width of view is 3.5 mm. c) *Sample 577C*. Metamorphic plagioclase containing fibrous and acicular kyanite is surrounded by a foliation of fine-grained garnet aggregates, fibrous kyanite and ilmenite. d) *Sample 577C.* Porphyroblastic garnet with rounded monazite inclusions, wrapped by fine-grained garnet aggregates and fibrous kyanite and ilmenite. e) *Sample Mann093.* Porphyroblastic K-feldspar surrounded by a fine-grained matrix of K-feldspar and quartz, which is wrapped by a layer of prismatic biotite and clinozoisite. f) Cross-polar image of figure e. g) *Sample DFC 387.* Garnet and plagioclase double corona around relict clinopyroxene. h) Cross-polar image of figure g. i) *Sample 441.* Fine-grained groundmass of clinopyroxene, garnet and metamorphic plagioclase. j) Cross-polar image of figure i. k) *Sample 542.* Garnet with plagioclase corona and rutile and

clinopyroxene. l) *Sample 542.* Poikiloblastic garnet with abundant quartz inclusions at the core. m) *Sample 532a.* Poikiloblastic garnet grain with hornblende corona. Width of view is 3.5 mm. n) Cross-polar image of figure m. Width of view is 3.5 mm. o) *Sample DFC 507.* Titanite corona on ilmenite with garnet, biotite and k-feldspar matrix. p) *Sample DFC 507.* Poikiloblastic garnet with biotite and titanite. q) *Sample Pe24.* Poikiloblastic hornblende with inclusions of quartz and titanite, wrapped by the biotite-K-feldspar foliation. Width of view is 8 mm. r) *Sample Pe24.* Poikiloblastic garnet with inclusions of quartz and hornblende and biotite growth particularly concentrated in strain shadows. Abundant titanite occurs in the matrix. Width of view is 8 mm. s) *Sample Pe24.* Euhedral titanite grains occurring in the matrix, aligned with the foliation, with hornblende and biotite. t) *Sample Pe17.* Double-corona of hornblende and garnet around clinopyroxene. Width of view is 4.5 mm. u) *Sample Pe17.* Hornblende corona around clinopyroxene. Width of view is 4.5 mm. v) *Sample Pe9.* Porphyroblastic garnet surrounded by hornblende. w) *Sample Pe9.* Hornblende coronas around garnet with plagioclase and titanite. Width of view is 3.5 mm. x) *Sample Pe9.* Thin titanite corona around rutile, in hornblende. Width of view is 2 mm.

Figure 4 - Chemical zoning profile and location of traverses for garnet samples

a) Sample Pe9
b) Sample 22b
c) Sample 577C

Figure 5

Calculated *P-T* pseudosection for sample Pe9. The yellow circle indicates the position of interpreted peak conditions, while the red arrow indicates the interpreted *P-T* path. Modal proportions of garnet is given in selected fields being represented by a thin dashed line. The position of the H_2O-in reaction is indicated by a thick black line. The mineral abbreviations used are those of Kretz (1983).

Figure 6-

a) Elemental map of sample 577C highlighting the contrast between relative Ca highs and lows. Yellow represents highs and black/blue represents lows.
b) Elemental map of sample 577C highlighting the contrast between relative Fe highs and lows. Yellow represents highs and black/blue represents lows.

Figure 7

Calculated *P-T* pseudosection for sample 577C. The yellow circle indicates the position of interpreted peak conditions, while the red arrow indicates the interpreted *P-T* path. Compositional isopleths for calcium in garnet are represented by long-dash line and calcium in plagioclase represented by short-dash lines. The position of the solidus is indicated by a thick black line. The mineral abbreviations used are those of Kretz (1983)

Figure 8

Diagrammatic representations of SHRIMP titanite age data from samples Pe9 and DFC 507. Tera-Wasserburg concordia plots using uncorrected isotope ratios are shown in (a) and (b), with some analyses excluded for reasons mentioned in the text. Anchor values for each regression line are also shown, along with their associated errors.

Figure 9

Diagrammatic representations of SHRIMP rutile age data from samples Pe9, DFC 387 and 441. $^{206}Pb/^{238}U$ weighted averages using 208-corrected age estimates are shown in (b), (d) and (e). Tera-Wasserburg concordia plots of the ^{208}Pb corrected $^{206}Pb/^{238}U$ vs. $^{207}Pb/^{235}U$ isotope ratio concordia are shown in (a) and (c), with some analyses excluded for reasons mentioned in the text. Anchor values for each regression line are also shown, along with their associated errors.

Figure 10

Diagrammatic representations of SHRIMP zircon age data from samples DFC 507 and 542. $^{206}Pb/^{238}U$ weighted averages using 204-corrected age estimates are shown in (a) and (b).

Figure 11-

Diagrammatic representation of *In-situ* LA-ICPMS monazite age data from sample 577C. A weighted average using $^{207}Pb/^{206}Pb$ age is shown in (a). A concordia plot of the $^{207}Pb/^{206}Pb$ vs. $^{238}U/^{206}Pb$ ratios is shown in (b).

Figure 12- Diagrammatic representation of diffusion-cooling modelling of garnet grains from sample Pe9

a) Xmg transect from core to rim is represented by black dots. The profile produced as a result of a user defined cooling history is represented by the red line.
b) Location of the traverse (core to rim)

c) Xmg transect from core to rim is represented by black dots. The profile produced as a result of a user defined cooling history is represented by the red line.
d) Location of the traverse (core to rim)

Figure 13- Diagrammatic representation of diffusion-cooling modelling of garnet grains from sample LH022b

a) Xmg transect from core to rim is represented by black dots. The profile produced as a result of a user defined cooling history is represented by the green/yellow line.
b) Location of the traverse (core to rim)
c) Xmg transect from core to rim is represented by black dots. The profile produced as a result of a user defined cooling history is represented by the red line.
d) Location of the traverse (core to rim)

Tables

Table 1 - Summary of Ediacaran-Cambrian geochronological data from the Western Musgrave Province

Age (Ma)	Method	Location	Reference
565 ± 9	K-Ar hornblende	Umutju region	*Scrimgeour et al.* [1999]
561 ± 11	SHRIMP U-Pb zircon (rim)	Umutju region	*Scrimgeour et al.* [1999]
494 ± 59	Sm-Nd mineral isochron	Eastern Mann Ranges	*Scrimgeour et al.* [1999]
559 ± 6	SHRIMP Th-Pb allanite (core)	Western Mann Ranges	*Gregory et al.* [2009]
551 ± 6	SHRIMP Th-Pb allanite (rim)	Western Mann Ranges	*Gregory et al.* [2009]
555 ± 7	SHRIMP U-Pb zircon (rim)	Western Mann Ranges	*Gregory et al.* [2009]
572 ± 7	SHRIMP U - Pb titanite	Bates region	*Raimondo et al.* [2009]
573 ± 14	SHRIMP U - Pb titanite	Bates region	*Raimondo et al.* [2009]
552 ± 12	SHRIMP U - Pb titanite (cooling)	Bates region	*Raimondo et al.* [2009]
539 ± 4	SHRIMP U - Pb titanite (cooling)	Bates region	*Raimondo et al.* [2009]
568 ± 12	SHRIMP U - Pb zircon (rim)	Bates region	*Raimondo et al.* [2010]
574 ± 5	SHRIMP U - Pb zircon (rim)	Bates region	*Raimondo et al.* [2010]
544 ± 7	SHRIMP U - Pb zircon (rim)	Western Mann Ranges	*Pfitzner* (2009)
580 ± 20	Electron Microprobe U-Pb Monazite	Angatja region	*Hallet* (2007)
521 ± 16	SHRIMP U - Pb titanite	Cockburn Shear Zone	This study
567 ± 18	SHRIMP U - Pb titanite	Umutju region	This study
496 ± 14	SHRIMP U - Pb rutile (cooling)	Cockburn Shear Zone	This study
490 ± 36	SHRIMP U - Pb rutile (cooling)	Western Mann Ranges	This study
502 ± 21	SHRIMP U - Pb rutile (cooling)	Western Mann Ranges	This study

Table 2- Representative mineral chemistry from all petrological groups

Sample	*577C*						*LH016B*						
Mineral	Gt (rim)	Gt (core)	Ilm	Ky	Ksp	Pl	Ilm	Bi	Pl	Ttn	Hbl	Gt (rim)	Gt
SiO2	36.82	35.56	0.06	36.80	63.81	63.78	0.16	35.71	63.74	29.37	38.92	35.75	35.62
TiO2	0.02	0.03	16.91	0.04	0.01	0.00	49.74	4.30	0.00	35.73	1.74	0.31	0.08
Al2O3	21.30	21.23	0.07	62.03	20.19	22.93	0.00	12.87	20.79	2.07	11.23	19.94	20.27
Cr2O3	0.00	0.05	0.03	0.00	0.00	0.00	0.03	0.00	0.00	0.02	0.04	0.00	0.00
FeO	26.33	26.77	75.26	1.05	0.30	0.01	46.32	23.48	0.10	1.03	22.95	28.04	28.97
MnO	2.25	2.16	0.05	0.02	0.04	0.01	0.51	0.06	0.00	0.06	0.11	1.69	1.59
MgO	9.11	9.17	0.33	0.00	0.00	0.00	0.05	8.76	0.01	0.00	6.20	1.37	1.62
ZnO	0.00	0.20	0.05	0.01	0.00	0.04	0.06	0.00	0.01	0.07	0.00	0.00	0.02
CaO	1.61	0.95	0.00	0.02	0.06	4.41	0.04	0.05	2.92	28.27	10.96	10.84	9.61
Na2O	0.04	0.02	0.02	0.00	1.45	9.48	0.04	0.04	10.37	0.04	1.79	0.00	0.00
K2O	0.00	0.00	0.02	0.00	13.86	0.08	0.01	9.49	0.24	0.02	1.93	0.02	0.01
Total	97.48	96.14	92.80	99.99	99.71	100.74	97.24	94.82	98.19	96.69	95.94	97.97	97.79
Si	1.23	1.18	0.00	1.23	2.12	2.12	0.01	1.19	2.12	0.98	1.30	1.19	1.19
Ti	0.00	0.00	0.42	0.00	0.00	0.00	1.25	0.11	0.00	0.89	0.04	0.01	0.00
Al	0.63	0.62	0.00	1.83	0.59	0.67	0.00	0.38	0.61	0.06	0.33	0.59	0.60
Cr	0.00	0.00	0.00	0.00	0.00	0.00	0.00	0.00	0.00	0.00	0.00	0.00	0.00
Fe2+	0.37	0.37	1.05	0.01	0.00	0.00	0.64	0.33	0.00	0.01	0.32	0.39	0.40
Mn2+	0.03	0.03	0.00	0.00	0.00	0.00	0.01	0.00	0.00	0.00	0.00	0.02	0.02
Mg	0.23	0.23	0.01	0.00	0.00	0.00	0.00	0.22	0.00	0.00	0.15	0.03	0.04
Zn	0.00	0.00	0.00	0.00	0.00	0.00	0.00	0.00	0.00	0.00	0.00	0.00	0.00
Ca	0.03	0.02	0.00	0.00	0.00	0.08	0.00	0.00	0.05	0.50	0.20	0.19	0.17
Na	0.00	0.00	0.00	0.00	0.02	0.15	0.00	0.00	0.17	0.00	0.03	0.00	0.00
K	0.00	0.00	0.00	0.00	0.15	0.00	0.00	0.10	0.00	0.00	0.02	0.00	0.00
Ni	0.00	0.00	0.00	0.00	0.00	0.00	0.00	0.00	0.00	0.00	0.00	0.00	0.00
T	2.51	2.46	1.49	3.07	2.89	3.03	1.91	2.32	2.96	2.45	2.39	2.43	2.42
X	12.00	12.00	3.00	5.00	8.00	8.00	3.00	11.00	8.00	5.00	23.00	12.00	12.00

Sample	*DFC 507*						*532a*			
Mineral	pl	ksp	bi	gt	ttn	hbl	gt (rim)	gt (core)	hbl	ttn
SiO2	65.41	65.25	35.95	37.78	30.71	39.46	38.19	38.11	44.35	30.44
TiO2	0.00	0.00	4.40	0.09	34.95	1.38	0.07	0.00	1.17	37.47
Al2O3	22.26	18.11	13.64	21.02	2.48	12.38	21.62	21.50	13.17	1.13
Cr2O3	0.04	0.07	0.00	0.02	0.08	0.00	0.08	0.00	0.03	0.03
FeO	0.08	0.00	24.78	25.55	1.26	24.31	21.12	20.39	12.59	0.34
MnO	0.01	0.06	0.18	1.99	0.02	0.33	0.56	0.61	0.10	0.03
MgO	0.00	0.00	6.77	1.01	0.00	4.90	5.88	6.12	12.00	0.00
ZnO	0.17	0.04	0.05	0.03	0.10	0.33	0.00	0.00	0.00	0.12
CaO	3.30	0.00	0.08	12.57	28.51	10.88	12.10	11.75	11.58	28.72
Na2O	10.13	1.03	0.05	0.08	0.07	1.89	0.04	0.01	1.84	0.03
K2O	0.24	15.06	9.28	0.00	0.05	1.99	0.00	0.00	0.51	0.02
Total	101.64	99.66	95.19	100.14	98.23	97.86	99.87	98.49	97.46	98.59
Si	2.18	2.17	1.20	1.26	1.02	1.31	2.96	2.98	6.50	1.01
Ti	0.00	0.00	0.11	0.00	0.88	0.03	0.00	0.00	0.13	0.93
Al	0.66	0.53	0.40	0.62	0.07	0.36	1.98	1.98	2.27	0.04
Cr	0.00	0.00	0.00	0.00	0.00	0.00	0.00	0.00	0.00	0.00
Fe2+	0.00	0.00	0.34	0.36	0.02	0.34	1.37	1.33	1.54	0.01
Mn2+	0.00	0.00	0.00	0.03	0.00	0.00	0.04	0.04	0.01	0.00
Mg	0.00	0.00	0.17	0.03	0.00	0.12	0.68	0.71	2.62	0.00
Zn	0.00	0.00	0.00	0.00	0.00	0.00	0.00	0.00	0.00	0.00
Ca	0.06	0.00	0.00	0.22	0.51	0.19	1.00	0.98	1.82	1.02
Na	0.16	0.02	0.00	0.00	0.00	0.03	0.01	0.00	0.52	0.00
K	0.00	0.16	0.10	0.00	0.00	0.02	0.00	0.00	0.10	0.00
Ni	0.00	0.00	0.00	0.00	0.00	0.00	0.00	0.00	0.00	0.00
Sum	3.06	2.88	2.33	2.51	2.50	2.43	8.05	8.03	15.53	3.03
No. Oxygens	8.00	8.00	11.00	12.00	5.00	23.00	12.00	12.00	23.00	5.00

Sample	*Pe9*					*Pe24*				
ID number	Pl	Hbl	Gt (rim)	Gt (core)	Ilm	Hbl	Gt (rims)	Gt (core)	Bi	Ksp
SiO2	63.23	41.90	38.39	38.80	0.0227	40.45	38.66	38.80	36.79	66.39
TiO2	0.01	2.06	0.06	0.06	44.1686	1.91	0.05	0.13	4.67	0.03
Al2O3	23.24	12.41	20.68	21.20	0.0003	12.87	19.88	19.79	14.46	18.30
Cr2O3	0.00	0.12	0.14	0.05	0.0575	0.07	0.13	0.00	0.12	0.04
FeO	0.20	16.11	25.43	24.09	49.5005	22.97	24.89	24.69	24.05	0.43
MnO	0.03	0.13	1.54	1.14	0.3182	0.33	2.20	1.61	0.16	0.03
MgO	0.00	10.20	4.51	5.01	0.9546	5.88	1.71	1.84	8.36	0.01
ZnO	0.11	0.06	0.02	0.05	0.1281	0.08	0.03	0.02	0.09	0.01
CaO	4.80	10.99	8.76	9.53	0.0106	10.94	12.86	13.54	0.09	0.07
Na2O	8.80	2.08	0.04	0.01	0.0867	1.43	0.03	0.02	0.07	0.68
K2O	0.43	1.64	0.00	0.03	0.025	2.04	0.01	0.00	9.13	15.39
Zr	0.03	0.03	0.00	0.00	0.0766					
Total	100.88	97.71	99.57	99.97	95.35	99.12	100.55	100.49	98.09	102.11
Si	2.10	1.39	1.28	1.29	0.001	1.35	1.29	1.29	1.22	2.21
Ti	0.00	0.05	0.00	0.00	1.106	0.05	0.00	0.00	0.12	0.00
Al	0.68	0.37	0.61	0.62	0.000	0.38	0.58	0.58	0.43	0.54
Cr	0.00	0.00	0.00	0.00	0.001	0.00	0.00	0.00	0.00	0.00
Fe2+	0.00	0.22	0.35	0.34	0.689	0.32	0.35	0.34	0.33	0.01
Mn2+	0.00	0.00	0.02	0.02	0.004	0.08	0.02	0.03	0.12	0.00
Mg	0.00	0.25	0.11	0.12	0.024	0.01	0.05	0.04	0.00	0.00
Zn	0.00	0.00	0.00	0.00	0.002	0.00	0.00	0.00	0.00	0.00
Ca	0.09	0.20	0.16	0.17	0.000	0.20	0.23	0.24	0.00	0.00
Na	0.14	0.03	0.00	0.00	0.001	0.02	0.00	0.00	0.00	0.01
K	0.00	0.02	0.00	0.00	0.000	0.02	0.00	0.00	0.10	0.16
Ni	0.00	0.00	0.00	0.00	0.001	0.00	0.00	0.00	0.00	0.00
Sum	3.03	2.54	2.54	2.56	1.829	2.43	2.53	2.53	2.33	2.94
No. oxygens	8.00	23.00	12.00	12.00	3	23.00	12.00	12.00	11.00	8.00

Table 3 – SHRIMP titanite age data

Sample DFC507					Isotope Ratios								Age (Ma)	
Spot name	U (ppm)	Th (ppm)	Spot	204Pb /206Pb	207Pb /206Pb	±%	208Pb /206Pb	±%	208Pb /248	±%	232Th /238U	±%	206Pb /238U	
507_1.1	15.8	2.1	0.14	0.0264	0.518	1.3	1.19	1.4	2.481	2.7	0.14	6.5	665	±44
507_2.1	19.2	4.1	0.22	0.0252	0.523	1.1	1.22	1.2	1.672	1.9	0.22	5.0	727	±38
507_3.1	6.2	0.8	0.13	0.0436	0.719	1.2	1.70	1.2	7.909	3.8	0.13	9.3	618	±120
507_4.1	23.7	1.8	0.08	0.0224	0.445	1.1	1.02	1.3	3.038	2.6	0.08	6.6	650	±29
507_5.1	4.2	3.0	0.72	0.0469	0.777	1.4	1.86	1.5	2.446	2.6	0.72	6.9	688	±217
507_6.1	12.2	4.3	0.36	0.0306	0.598	1.1	1.40	1.2	1.541	1.9	0.36	4.9	732	±53
507_7.1	22.4	5.3	0.25	0.0116	0.370	1.4	0.83	1.6	0.673	2.0	0.25	4.9	703	±23
507_9.1	20.3	2.5	0.13	0.0212	0.481	1.8	1.08	2.0	2.594	2.5	0.13	6.2	733	±32
507_8.1	16.4	2.8	0.17	0.0238	0.518	1.3	1.20	1.4	1.942	2.4	0.17	5.9	704	±40
507_10.1	7.9	4.4	0.58	0.0335	0.663	1.2	1.63	1.3	1.469	1.8	0.58	5.2	904	±83
507_11.1	12.5	2.2	0.18	0.0298	0.618	1.3	1.40	1.4	3.064	3.0	0.18	7.3	821	±66

Sample Pe9					Isotope Ratios								Age (Ma)	
Spot	U (ppm)	Th (ppm)	232Th /238U	204Pb /206Pb	207Pb /206Pb	±%	208Pb /206Pb	±%	208Pb /248	±%	232Th /238U	±%	206Pb /238U	
PE9_1.1	30.6	55.8	1.88	0.0173	0.332	1.2	1.08	1.8	0.108	1.8	1.88	3.9	548	±14
PE9_1.2	29.7	42.0	1.46	0.0132	0.294	1.3	0.89	1.3	0.116	1.2	1.46	3.4	561	±14
PE9_2.1	57.9	27.6	0.49	0.0115	0.281	1.8	0.69	1.2	0.231	1.2	0.49	3.4	567	±42
PE9_3.1	30.7	38.2	1.29	0.0074	0.214	1.6	0.70	1.5	0.085	1.4	1.29	3.5	552	±17
PE9_4.1	19.4	69.8	3.72	0.0158	0.359	1.4	1.48	2.0	0.083	1.0	3.72	3.9	610	±14
PE9_5.1	33.7	48.1	1.48	0.0131	0.304	1.1	0.94	1.1	0.120	1.0	1.48	3.3	591	±19
PE9_6.1	44.3	36.5	0.85	0.0149	0.280	1.0	0.76	1.1	0.159	1.0	0.85	3.2	530	±34
PE9_7.1	22.5	71.7	3.29	0.0126	0.353	1.2	1.40	1.2	0.084	0.9	3.29	3.3	620	±14

PE9_8.1	13.3	53.0	4.13	0.0193	0.488	1.4	1.72	1.3	0.108	1.0	4.13	3.5	722	±17
PE9_9.1	36.3	40.2	1.15	0.0125	0.271	1.1	0.79	1.1	0.124	1.1	1.15	3.3	565	±16
PE9_10.1	35.9	33.1	0.95	0.0164	0.323	1.1	0.87	1.1	0.165	1.1	0.95	3.3	537	±27
PE9_11.1	37.6	42.4	1.17	0.0139	0.314	1.1	0.89	1.2	0.134	1.1	1.17	3.3	553	±22
PE9_12.1	15.6	48.2	3.19	0.0209	0.404	1.3	1.45	1.3	0.101	1.0	3.19	3.6	561	±19
PE9_13.1	30.2	50.9	1.74	0.0205	0.342	1.2	1.07	1.2	0.113	2.0	1.74	3.3	502	±20
PE9_14.1	28.7	41.6	1.50	0.0161	0.354	1.2	1.04	1.2	0.127	1.1	1.50	3.3	560	±29
PE9_15.1	25.3	60.0	2.45	0.0167	0.344	1.2	1.22	1.1	0.097	1.6	2.45	3.3	575	±15
PE9_16.1	19.0	50.7	2.75	0.0222	0.422	1.3	1.38	1.2	0.106	1.0	2.75	3.4	540	±32
PE9_17.1	38.1	32.1	0.87	0.0133	0.297	1.0	0.79	1.1	0.176	1.1	0.87	3.3	578	±26
PE9_18.1	23.1	107.1	4.79	0.0134	0.317	1.3	1.66	1.1	0.063	0.9	4.79	3.3	574	±15
PE9_19.1	16.5	67.5	4.23	0.0217	0.400	1.2	1.66	1.1	0.086	1.5	4.23	3.6	547	±13
PE9_20.1	43.0	44.9	1.08	0.0151	0.291	1.0	0.84	1.1	0.136	1.0	1.08	3.2	545	±16
PE9_21.1	43.2	33.5	0.80	0.0125	0.281	0.9	0.75	0.9	0.178	0.9	0.80	3.2	584	±21
PE9_22	35.0	53.8	1.59	0.0155	0.320	1.1	0.97	1.1	0.114	1.0	1.59	3.2	563	±20
PE9_23.1	43.2	31.9	0.76	0.0126	0.290	1.0	0.75	1.1	0.176	1.1	0.76	3.3	576	±24
PE9_24.1	18.2	41.9	2.38	0.0115	0.302	1.7	1.09	1.5	0.084	3.4	2.38	4.3	580	±10
PE9_25.1	23.6	47.7	2.08	0.0213	0.380	1.2	1.21	1.2	0.115	1.0	2.08	3.3	525	±19
PE9_26.1	38.9	42.6	1.13	0.0050	0.187	1.4	0.63	1.4	0.078	1.3	1.13	3.3	542	±15
PE9_27.1	19.7	92.0	4.82	0.0131	0.337	1.3	1.68	1.1	0.069	0.9	4.82	3.4	609	±19

Table 4 – SHRIMP rutile age data

Sample 441				**Isotope Ratios**								**Age (Ma)**	
Spot	ppm U	ppm Th	208-corr 206Pb	207Pb /206Pb	±%	208Pb /206Pb	±%	206Pb /254	±%	206Pb /270	±%	206Pb /238U (^{208}Pb-corr)	
441-1.1	3.2	0.0084	0.233	0.588	6.1	1.42	5	0.392	17.6	0.526	15.0	516	±480
441-2.1	4.0	0.0048	0.416	0.675	3.2	1.63	3	0.743	15.5	1.028	14.9	745	±1439
441-3.1	5.6	-0.0028	0.420	0.220	6.8	0.42	13	0.309	6.2	0.246	4.8	536	±45
441-4.1	6.9	0.0599	0.448	0.159	12.2	0.30	16	0.282	2.6	0.200	2.7	472	±34
441-5.1	2.4	0.0061	0.177	0.260	12.1	0.52	13	0.143	7.2	0.224	3.4	537	±92
441-6.1	4.1	0.0067	0.309	0.476	6.2	1.09	4	0.312	11.8	0.376	10.7	540	±294
441-7.1	4.6	0.0205	0.297	0.170	4.7	0.29	11	0.226	3.0	0.197	4.7	472	±47
441-8.1	4.5	0.0017	0.315	0.163	15.4	0.29	12	0.237	6.0	0.210	5.9	507	±221
441-9.1	5.6	0.0064	0.373	0.200	4.0	0.38	12	0.205	10.0	0.205	5.1	483	±51
441-10.1	3.9	0.0070	0.264	0.195	8.7	0.32	15	0.232	6.6	0.207	5.0	490	±42
441-11.1	3.0	0.0137	0.195	0.254	7.4	0.51	12	0.164	10.2	0.209	6.8	478	±99
441-12.1	4.8	0.0071	0.376	0.557	1.8	1.43	3	0.681	19.0	0.632	11.0	565	±661
441-12.2	3.5	0.0114	0.266	0.601	4.9	1.34	6	0.384	18.4	0.504	18.2	544	±467
441-13.1	3.6	0.0010	0.259	0.294	8.6	0.59	12	0.269	10.1	0.247	3.2	522	±421
441-14.1	3.2	0.0027	0.212	0.431	8.1	0.99	9	0.394	10.3	0.333	10.8	486	±334

Sample Pe9				**Isotope Ratios**								**Age (Ma)**
Spot	ppm U	ppm Th	208-corr 206Pb	207Pb /206Pb	±%	208Pb /206Pb	±%	206Pb /254	±%	206Pb /270	±%	206Pb /238U (^{208}Pb-corr)

PE9-1.1	6.4	0.0031	0.425	0.118	15.0	0.17	15	0.164	2.0	0.177	2.3	479	±16
PE9-1.2	5.0	0.0151	0.368	0.207	9.8	0.37	20	0.120	2.3	0.201	4.8	534	±71
PE9-3.1	16.2	0.0143	1.123	0.140	9.2	0.19	15	0.285	3.1	0.206	3.2	499	±25
PE9-4.1	11.0	0.0037	0.825	0.085	4.7	0.12	4	0.232	4.7	0.205	2.0	540	±15
PE9-5.1	5.8	0.0020	0.433	0.135	7.4	0.18	5	0.107	2.3	0.181	2.3	536	±52
PE9-6.1	6.3	0.0013	0.438	0.105	4.7	0.11	11	0.132	9.2	0.174	4.2	503	±33
PE9-7.1	5.1	0.0229	0.394	0.118	4.7	0.18	5	0.130	6.0	0.192	2.5	555	±24
PE9-9.1	5.0	0.0160	0.357	0.133	13.3	0.19	12	0.156	7.2	0.188	4.6	517	±38
PE9-10.1	10.5	0.0068	0.644	0.086	4.2	0.08	5	0.257	2.1	0.175	1.9	447	±14
PE9-11.1	5.3	0.0186	0.412	0.513	7.1	1.23	7	0.290	11.5	0.425	9.7	554	±382
PE9-12.1	7.2	0.0448	0.569	0.128	4.1	0.16	15	0.122	2.0	0.192	2.2	566	±22
PE9-13.1	6.2	0.0066	0.418	0.136	4.6	0.21	12	0.189	4.4	0.189	3.7	489	±36
PE9-14.1	4.5	0.0056	0.320	0.162	4.3	0.23	11	0.163	2.5	0.193	2.7	512	±42
PE9-15.1	4.3	0.0122	0.331	0.139	9.8	0.20	16	0.149	8.2	0.193	2.8	551	±36

Sample DFC387				**Isotope Ratios**								**Age (Ma)**	
Spot	ppm U	ppm Th	208-corr 206Pb	207Pb /206Pb	±%	208Pb /206Pb	±%	206Pb /254	±%	206Pb /270	±%	206Pb /238U (^{208}Pb-corr)	
387-1.1	3.0	0.0056	0.252	0.250	9.2	0.46	15	0.137	3.1	0.239	3.1	602	±105
387-2.1	6.6	0.0121	0.439	0.191	9.0	0.33	14	0.288	4.6	0.207	2.8	483	±52
387-3.1	3.4	0.0075	0.259	0.192	4.7	0.34	9	0.125	7.8	0.206	3.1	555	±60
387-4.1	3.0	0.0029	0.212	0.222	5.0	0.49	8	0.129	5.2	0.207	5.4	510	±139
387-5.1	4.0	0.0032	0.277	0.180	7.8	0.32	15	0.169	2.7	0.199	2.8	505	±59
387-6.1	8.0	0.0023	0.546	0.188	9.9	0.32	17	0.334	4.8	0.221	2.2	492	±30
387-7.1	6.2	0.0066	0.429	0.659	2.8	1.60	3	0.940	13.1	0.744	11.7	496	±349
387-8.1	2.9	0.0088	0.223	0.191	11.1	0.36	11	0.114	5.2	0.202	3.2	553	±101
387-9.1	4.0	0.0161	0.303	0.224	11.9	0.40	15	0.196	4.9	0.226	2.8	545	±72

387-10.1	5.1	0.0012	0.379	0.161	10.4	0.28	14	0.239	2.6	0.220	2.5	537	±180
387-11.1	3.6	0.0145	0.284	0.185	12.8	0.27	21	0.118	3.1	0.203	6.5	573	±66
387-12.1	4.1	0.0050	0.309	0.191	7.8	0.34	14	0.125	2.9	0.206	5.7	549	±68
387-13.1	2.8	0.0067	0.193	0.226	9.9	0.44	15	0.118	6.6	0.196	3.2	505	±69
387-14.1	4.4	0.0026	0.288	0.179	10.1	0.31	13	0.181	2.8	0.193	2.9	477	±36
387-15.1	6.8	0.0081	0.450	0.156	10.1	0.23	20	0.309	3.1	0.204	2.7	476	±45

Table 5 – SHRIMP zircon age data

Sample 542			**Isotope Ratios**										
Spot	ppm U	ppm Th	238U /206Pb	±%	207Pb /206Pb	±%	207Pb /235U	±%	206Pb /238U	±%	err corr	232Th /238U	±%
542-1.1	48	68	6.94	2.1	0.0708	4.9	1.41	5.4	0.144	2.1	0.4	1.46	0.47
542-1.2	20	27	5.24	2.6	0.0836	3.4	2.20	4.3	0.191	2.6	0.6	1.37	0.70
542-2.1	38	38	5.31	2.2	0.0811	2.3	2.10	3.2	0.188	2.2	0.7	1.04	0.88
542-3.1	36	54	5.63	3.0	0.0727	4.8	1.78	5.7	0.178	3.0	0.5	1.56	0.55
542-3.2	37	57	4.94	5.1	0.0912	5.2	2.54	7.3	0.202	5.1	0.7	1.60	0.62
542-4.1	18	23	5.16	2.8	0.0819	7.0	2.19	7.5	0.194	2.8	0.4	1.31	0.78
542-5.1	80	100	5.27	1.8	0.0772	1.5	2.02	2.4	0.190	1.8	0.8	1.30	0.37
542-10.1	23	33	5.23	2.5	0.0778	6.8	2.05	7.3	0.191	2.5	0.3	1.43	0.65
542-6.1	68	82	5.20	1.9	0.0823	1.7	2.18	2.6	0.192	1.9	0.7	1.24	0.40
542-7.1	20	28	5.33	2.6	0.0781	4.2	2.02	4.9	0.187	2.6	0.5	1.41	0.70
542-8.1	50	71	6.31	2.0	0.0763	5.1	1.67	5.5	0.158	2.0	0.4	1.47	0.45
542-9.1	39	44	5.33	2.2	0.0796	3.0	2.06	3.7	0.188	2.2	0.6	1.18	0.52
542-11.1	27	38	7.54	2.4	0.0705	6.1	1.29	6.6	0.133	2.4	0.4	1.48	0.62
542-12.1	77	77	5.14	1.9	0.0829	1.5	2.22	2.4	0.194	1.9	0.8	1.04	0.39
542-12.2	78	78	5.08	1.9	0.0788	1.5	2.14	2.4	0.197	1.9	0.8	1.04	0.40
542-13.1	73	86	5.10	1.9	0.0809	1.6	2.19	2.5	0.196	1.9	0.8	1.22	0.38
542-14.1	76	108	5.18	1.9	0.0800	1.8	2.13	2.6	0.193	1.9	0.7	1.47	0.37
542-14.2	76	108	5.09	1.9	0.0781	2.2	2.11	2.9	0.196	1.9	0.6	1.47	0.38

Sample DFC507			**Isotope Ratios**										
Spot	ppm U	ppm Th	238U /206Pb	±%	207Pb /206Pb	±%	207Pb /235U	±%	206Pb /238U	±%	err corr	232Th /238U	±%
507-1.1	108	83	5.56	1.7	0.0776	1.5	1.92	2.3	0.180	1.7	0.8	0.79	0.34
507-2.1	138	92	5.69	1.7	0.0739	1.3	1.79	2.1	0.176	1.7	0.8	0.69	0.30
507-3.1	27	30	5.83	2.3	0.0841	3.9	1.99	4.6	0.172	2.3	0.5	1.15	0.58
507-4.1		0	0.08	21.2	0.7223	6.2	1185.75	22.1	11.906	21.2	1.0	0.76	9.34
507-5.1	126	95	5.32	1.7	0.0790	1.1	2.05	2.0	0.188	1.7	0.8	0.78	0.31
507-6.1	44	42	5.89	2.1	0.0861	13.0	2.02	13.2	0.170	2.1	0.2	0.99	0.50
507-7.1	19	23	6.43	2.8	0.0892	5.3	1.91	6.0	0.155	2.8	0.5	1.30	1.47
507-8.1	66	109	5.79	1.9	0.0826	1.9	1.97	2.7	0.173	1.9	0.7	1.71	1.76
507-9.1	42	43	5.58	2.1	0.0795	2.3	1.96	3.1	0.179	2.1	0.7	1.07	0.86
507-9.2	139	85	5.61	1.7	0.0754	1.1	1.85	2.0	0.178	1.7	0.8	0.63	0.31
507-10.1	18	21	5.60	2.8	0.0854	4.8	2.10	5.6	0.179	2.8	0.5	1.20	0.81
507-10.2	236	131	5.46	1.9	0.0749	0.9	1.89	2.1	0.183	1.9	0.9	0.57	0.40
507-11.1	125	66	5.63	1.7	0.0754	1.3	1.85	2.2	0.178	1.7	0.8	0.54	0.36
507-11.2	12	19	5.34	3.4	0.1023	9.3	2.64	9.9	0.187	3.4	0.3	1.71	0.95
507-12.1	145	83	5.69	1.7	0.0765	1.2	1.85	2.1	0.176	1.7	0.8	0.59	0.31
507*-13.1	75	65	5.56	1.9	0.0763	1.9	1.89	2.7	0.180	1.9	0.7	0.90	0.41
507-14.1	70	61	5.77	1.9	0.0739	1.8	1.77	2.7	0.173	1.9	0.7	0.89	0.44
507-15.1	66	63	5.52	2.9	0.0760	1.5	1.90	3.2	0.181	2.9	0.9	0.98	0.64
507-16.1	105	90	5.15	2.5	0.0770	1.6	2.06	3.0	0.194	2.5	0.8	0.88	1.52

Table 6- LA-ICPMS zircon trace element data

Sample Pe24

Spot	Ca	Ti	Fe	Zr	La	Ce	Nd	Sm	Eu	Gd	Tb	Dy	Ho	Er	Yb	Lu	Hf
Spot 1	<271	7.8	16.25	524077	0.137	1.383	0.38	<0.3	0.094	0.92	0.64	8.46	3.28	13.27	24.42	3.98	13694
Spot 2	<237	5.8	43.55	485021	0.101	0.708	<0.25	<0.3	0.094	1.24	0.645	7.73	2.54	8.81	11.12	1.58	15042
Spot 3	<318	8.33	129.1	479391	0.672	4.55	1.15	0.6	0.138	1.68	0.573	9.27	3.44	15.89	31.9	6.42	12256
Spot 4	<350	29.2	162.8	543506	62.36	828.68	47.13	9.99	1.94	14.61	2.27	20.48	6.18	22.33	35.51	5.34	14480
Spot 5	<354	129	1448	514138	3.89	23.75	9.54	2.2	0.3	4.38	1.2	16.55	5.5	23.08	50.01	7.62	13873
Spot 6	<505	13.9	119	462835	0.381	3.53	0.84	<0.6	0.28	1.51	0.903	12.69	5.01	22.85	44.37	8.53	13824
Spot 7	<308	9.47	58.44	548096	2.58	15.53	4.08	1.98	0.34	3.84	1.02	12.36	4.43	16.77	34.81	5.38	14819
Spot 8	2143	16.4	845.9	501438	32.32	265.8	58.3	19.4	4.01	24.48	5.87	55.23	19.1	90	228.87	45.16	17389
Spot 9	265	6.46	87.37	507595	1.51	5.64	1.42	0.77	0.159	1.94	0.721	16.47	8.5	44.71	124.09	24.9	16225
Spot 10	<286	7.97	406.5	515912	2.6	27.79	3.85	1.47	0.221	2.99	1.048	14.52	5.61	24.56	49.04	8.91	14201
Spot 11	709	12.0	1271	541331	2.15	8	4.69	1.78	0.34	3.69	1.21	15.76	6.18	22.7	39.7	7.12	14954
Spot 12	<225	14.3	215.4	511529	20.93	15.33	15.79	3.73	0.394	6	2.14	28.21	11.9	62.91	169.58	37.65	14144
Spot 13	<243	8.82	220	499940	1.8	23.39	4.5	2.06	0.466	5.32	1.644	20.6	8.19	41	107.07	21.4	17087
Spot 14	<21	8.85	104	492323	2.36	19.92	7.21	3.39	0.866	8.09	3.06	33.9	10.7	35.96	46.69	6.31	16168
Spot 15	609	32.1	730	513216	8.89	23.67	11.36	3.91	0.73	7.18	2.46	27.2	8.83	34.1	73.92	11.5	13899
Spot 16	291	5.9	106	492569	0.573	8.44	2.1	1.14	0.156	5.18	1.75	24.0	9.75	47.57	116.13	23.09	15773
Spot 17	<239	8.22	320	470842	2.5	16.63	5.42	3.23	0.504	6.2	2.2	25.5	9.96	46.59	113.83	23.74	12247
Spot 18	1012	17.1	520	468326	6.45	298.41	11.78	3.46	0.605	5.57	1.79	19	7.74	36.29	88.01	17.83	12200
Spot 19	<225	6.62	83.85	493772	0.491	6.06	0.82	0.57	0.208	2.98	1.282	16	7.27	36.28	100.16	18.98	12971
Spot 20	<220	14.3	179	493783	4.79	197.72	10.62	5.84	0.914	20.47	6.84	82.6	31.9	142.52	318.14	57.76	12805
Spot 21	<210	16.0	515	494734	17.4		37.92	12.4	2.51	18.27	3.95	37.1	12.2	52.54	120.16	23.64	15121

Table 7- LA-ICPMS titanite trace element data

Sample Pe24

Spot name	Ca	Ti	Fe	Zr	La	Ce	Nd	Sm	Eu	Gd	Tb	Dy	Ho	Er	Yb	Lu	Hf
Spot 1	213224	187413	8790	214.15	196.02	1065	1441	614	134	648	114.65	616.14	98.94	195.23	102.68	9.1	12.32
Spot 2	194345	176261	7637	146.2	64.61	337	399	194	56	243	49.24	280.44	44.44	89.08	61.74	6.64	8.43
Spot 3	187082	178528	6912	184.56	146.37	804	981	429	104	473	86.14	469.65	78.9	168.04	110.79	11.28	10.06
Spot 4	190799	172925	6600	151.99	81.33	450	492	235	67	288	58.94	346.99	58.48	126.08	94.69	10.39	7.79
Spot 5	180254	169280	6356	156.39	108.61	607	665	304	82	354	67.95	378.63	62.14	129.28	86.35	9.17	9.33
Spot 6	178846	167326	6346	137.43	82.21	463	526	251	70	300	59.42	333.86	54.57	107.53	60.98	6.05	7.85
Spot 7	177392	165353	5989	147.51	81.89	443	449	211	60	256	53.5	317.49	54.68	117.76	79.39	8.26	8.07
Spot 8	180281	166771	6078	126.74	69.12	364	396	191	54	237	48.55	287.08	47.9	103.83	83	9.28	5.61
Spot 9	184432	172170	6350	133.26	60.01	360	427	217	62	279	57.46	328.83	54.77	108.83	60.96	5.96	6.89
Spot 10	184678	175008	5996	161	86.69	461	516	237	68	287	55.58	307.73	49.64	101.97	68.49	7.84	7.74
Spot 11	182114	177548	6525	212.95	197.31	1062	1198	493	111	536	97.6	544.91	94.61	199.65	133.39	14.67	12.03
Spot 12	258962	299843	14578	396	178.96	833	1000	468	101	607	107.68	546.62	83.5	144.83	59.07	5.54	11.12
Spot 13	199414	244715	9677	425.79	254.68	1177	1278	515	100	573	88.29	423.79	64.04	120.06	50.88	4.89	9.72
Spot 14	193794	234122	8444	288.96	94.14	398	402	181	45	258	48.99	278.23	49.88	111.05	66.16	7.67	7.2
Spot 15	198634	244630	8463	294.14	134.31	622	674	302	68	379	68.01	365.28	66.77	139.78	73.42	8.15	8.14
Spot 16	197168	239686	8138	282.48	99.53	431	412	196	49	272	51.95	292.39	46.54	92.89	43.56	4.44	5.84
Spot 17	199463	247990	8727	328.93	134.87	644	686	295	55	357	66.02	356.24	64.94	134.61	83.23	10.23	8.32
Spot 18	188105	248558	7462	428.84	296.12	1292	1262	477	107	548	94.57	527.7	98.06	221.58	145.5	18.26	10.97
Spot 19	198562	279028	10077	465.16	295.05	1400	1507	618	120	709	112.76	584.79	93.99	176.53	71.21	7.68	8.14
Spot 20	223006	284080	10170	350.58	121.73	544	535	252	65	350	69.81	396.7	68.42	139.8	82.18	10.03	7.42
Spot 21	238863	277667	10145	322.39	103.15	439	437	212	59	305	59.57	319.64	51.46	97.19	45.61	4.14	8.2
Spot 22	226950	281037	9657	422.23	205.98	848	740	313	80	425	81.91	501.56	95.86	242.21	216.96	30.7	10.05

Table 8 - Summary of thermometry parameters

Zr in sphene thermometer (Hayden et al., 2008)				
Zr conc. Range ppm	Calculated *T* range @ 10 Kbars (ºC)	Ave Zr conc.(ppm 1 σ)	Calculated average *T* ± 1σ	Calculated average *T* (ºC ± 1σ ± 1 Kbar)
126.74 - 214.15	757 - 785	156.32 ± 13	768 ± 4	768 ± 15

Ti in zircon thermometer (Watson et al., 2006)				
Ti conc. range (ppm)	Calculated *T* range (ºC)	Ave Ti conc. (ppm, 1 sigma)	Calculated average *T* (ºC, ± 1 sigma)	Calculated average *T* (ºC, ± max. *T* range)
5.9-17.17	696-790	9.2 ± 0.9	733.7 ± 10	733.7 ± 23

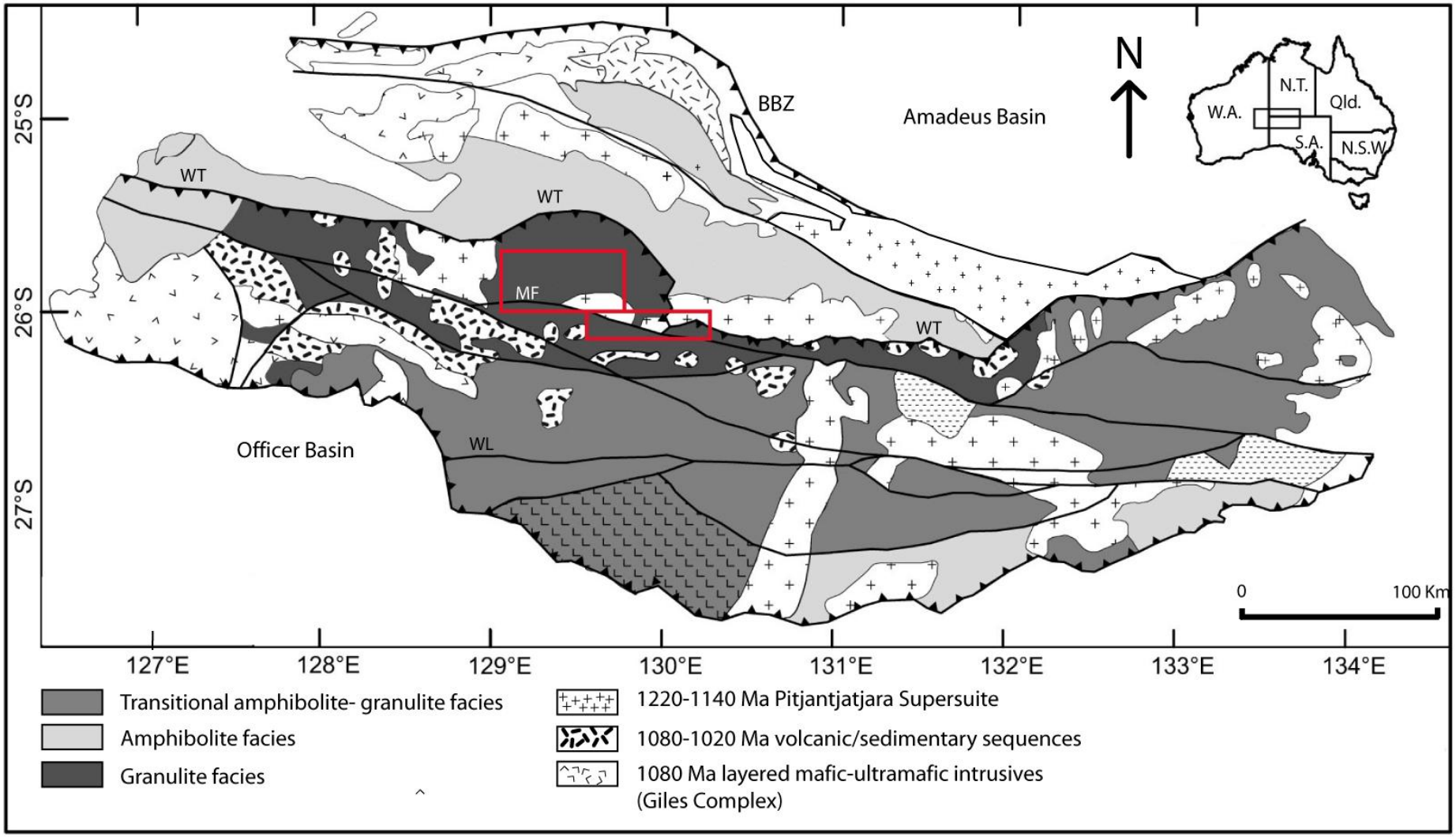
25°S
26°S
27°S
127°E
128°E
129°E
130°E
131°E
132°E
133°E
134°E
N
BBZ
Amadeus Basin
WT
WT
WT
MF
WT
Officer Basin
WL
N.T.
Qld.
W.A.
S.A.
N.S.W.
0
100 Km
Transitional amphibolite- granulite facies
Amphibolite facies
Granulite facies
1220-1140 Ma Pitjantjatjara Supersuite
1080-1020 Ma volcanic/sedimentary sequences
1080 Ma layered mafic-ultramafic intrusives
(Giles Complex)

Figure 1

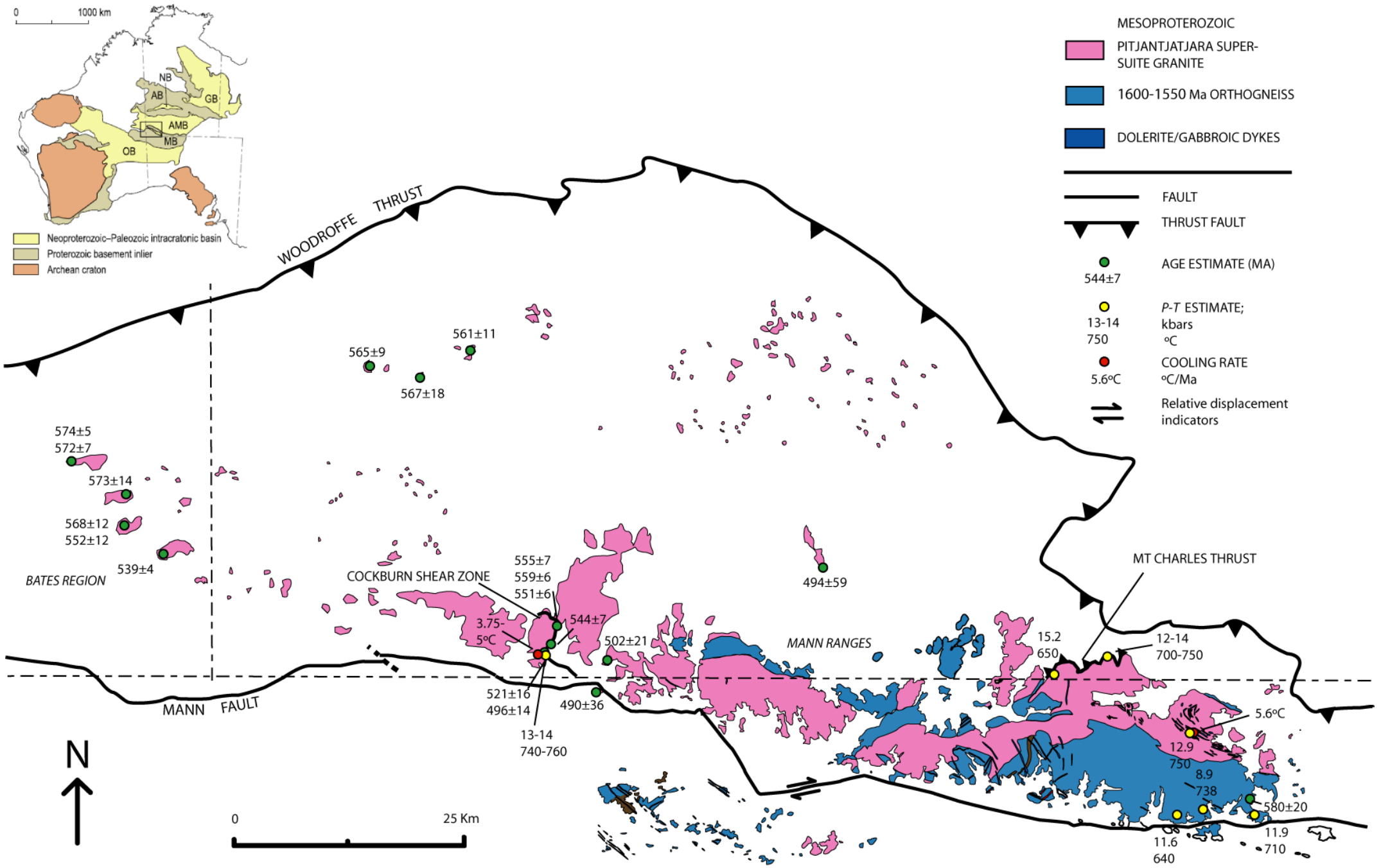
0
1000 km
NB
AB
GB
AMB
MB
OB
Neoproterozoic–Paleozoic intracratonic basin
Proterozoic basement inlier
Archean craton
MESOPROTEROZOIC
PITJANTJATJARA SUPER-SUITE GRANITE
1600-1550 Ma ORTHOGNEISS
DOLERITE/GABBROIC DYKES
FAULT
THRUST FAULT
544±7
AGE ESTIMATE (MA)
13-14
750
P-T ESTIMATE; kbars °C
5.6°C
COOLING RATE °C/Ma
Relative displacement indicators
WOODROFFE THRUST
561±11
565±9
567±18
574±5
572±7
573±14
568±12
552±12
539±4
BATES REGION
COCKBURN SHEAR ZONE
555±7
559±6
551±6
544±7
3.75-5°C
502±21
494±59
MANN RANGES
MT CHARLES THRUST
15.2
650
12-14
700-750
MANN FAULT
521±16
496±14
490±36
13-14
740-760
5.6°C
12.9
750
8.9
738
580±20
11.6
640
11.9
710
N
0
25 Km

Figure 2

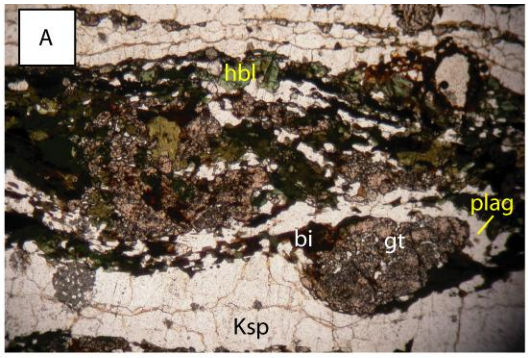
A
hbl
plag
bi
gt
Ksp

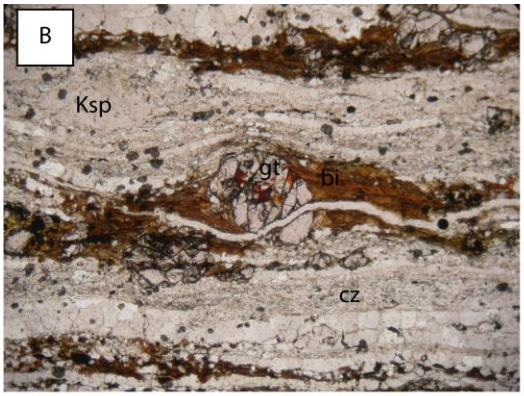
B
Ksp
gt
bi
cz

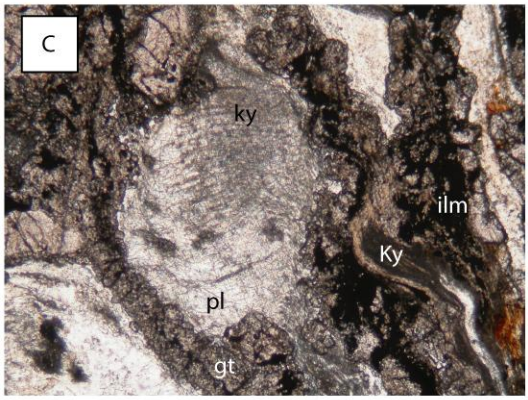
C
ky
ilm
Ky
pl
gt

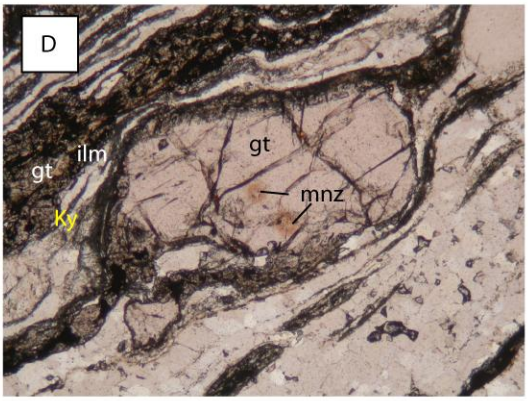
D
gt
ilm
gt
mnz
Ky

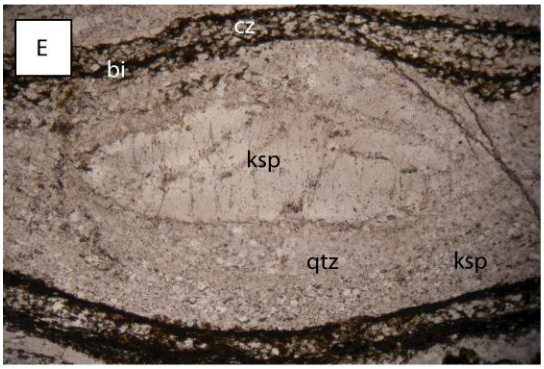
E
cz
bi
ksp
qtz
ksp


F

Figure 3

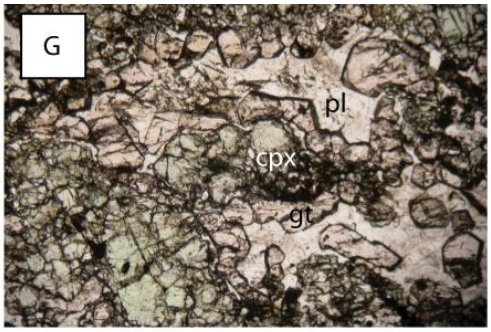
G
pl
cpx
gt

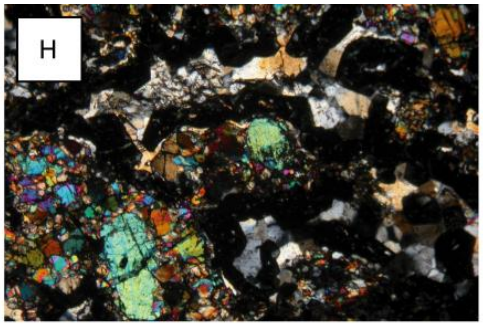
H

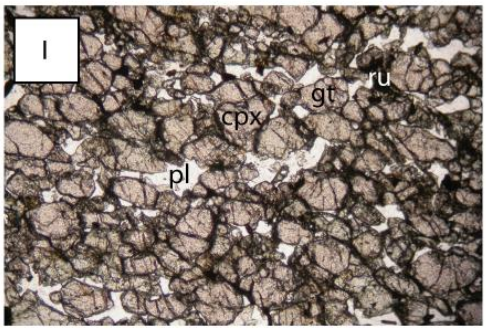
I
ru
gt
cpx
pl

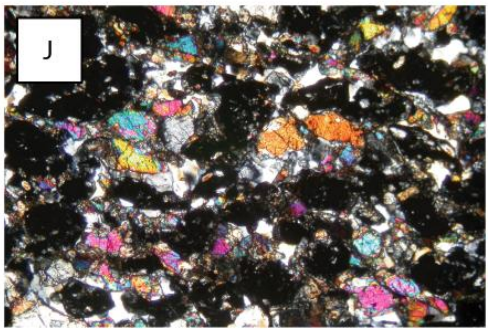
J

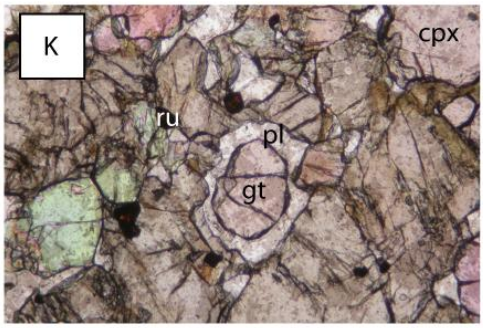
K
cpx
ru
pl
gt

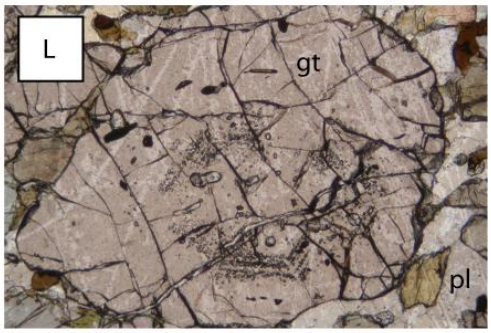
L
gt
pl

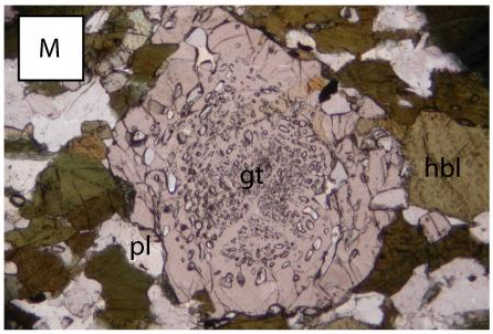
M
gt
hbl
pl

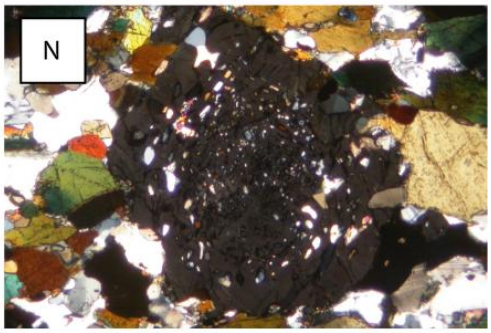
N

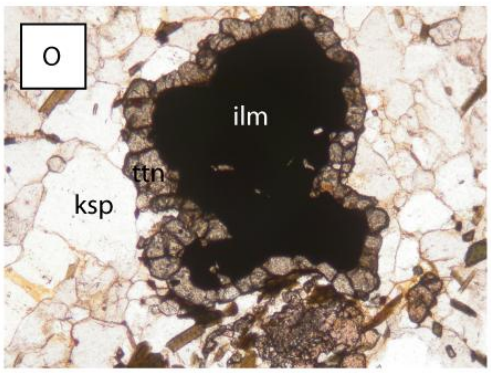
O
ilm
ttn
ksp

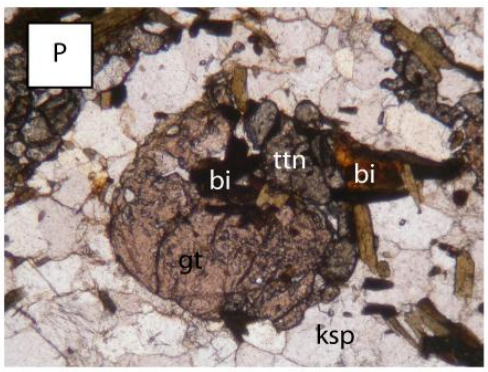
P
ttn
bi
bi
gt
ksp

Figure 3

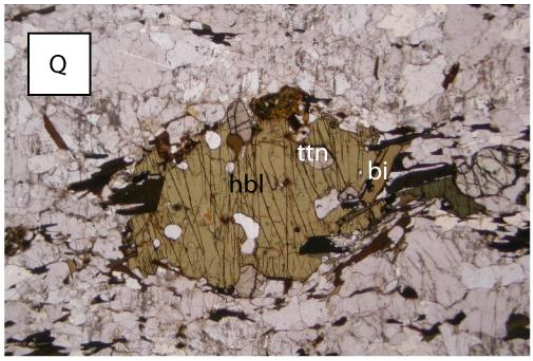
Q
ttn
bi
hbl


R
gt
bi
hbl

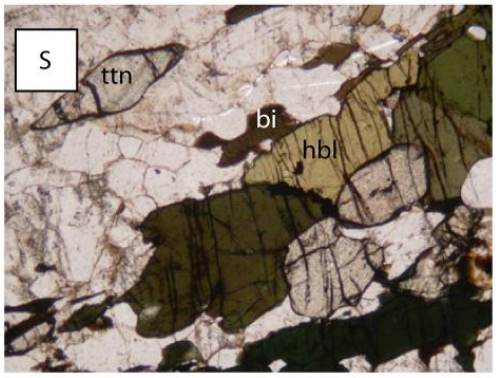
S
ttn
bi
hbl

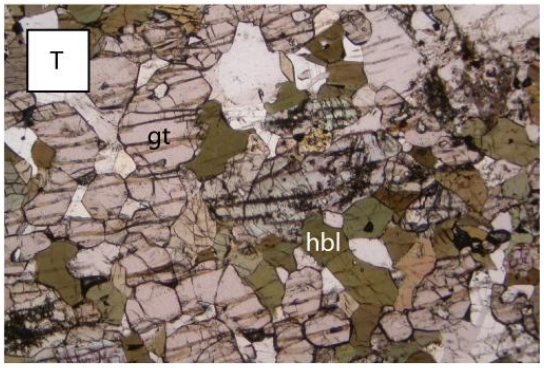
T
gt
hbl

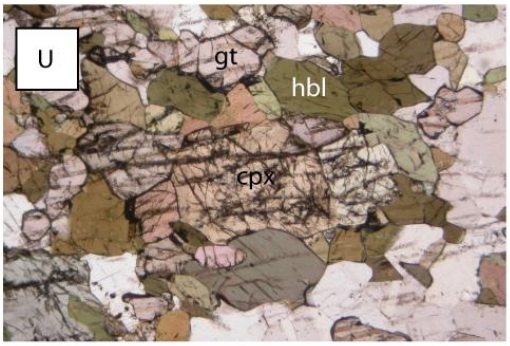
U
gt
hbl
cpx

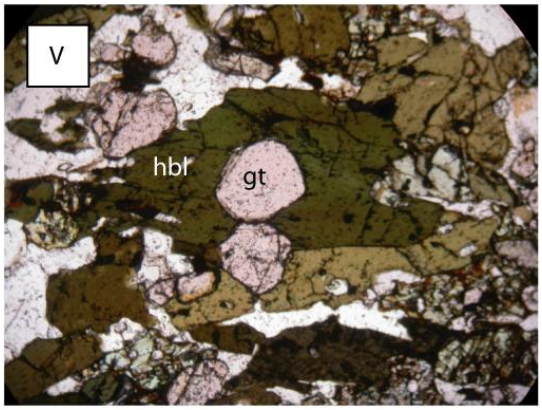
V
hbl
gt

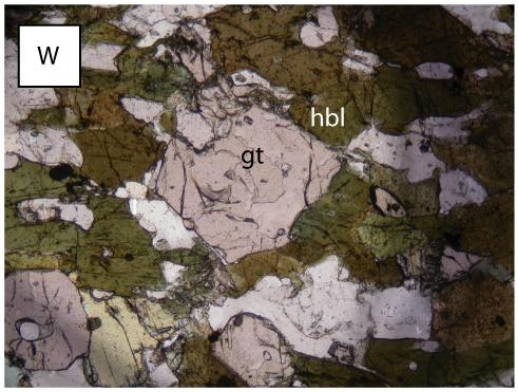
W
hbl
gt

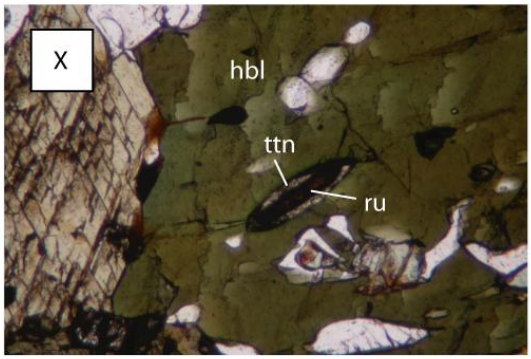
X
hbl
ttn
ru

Figure 3

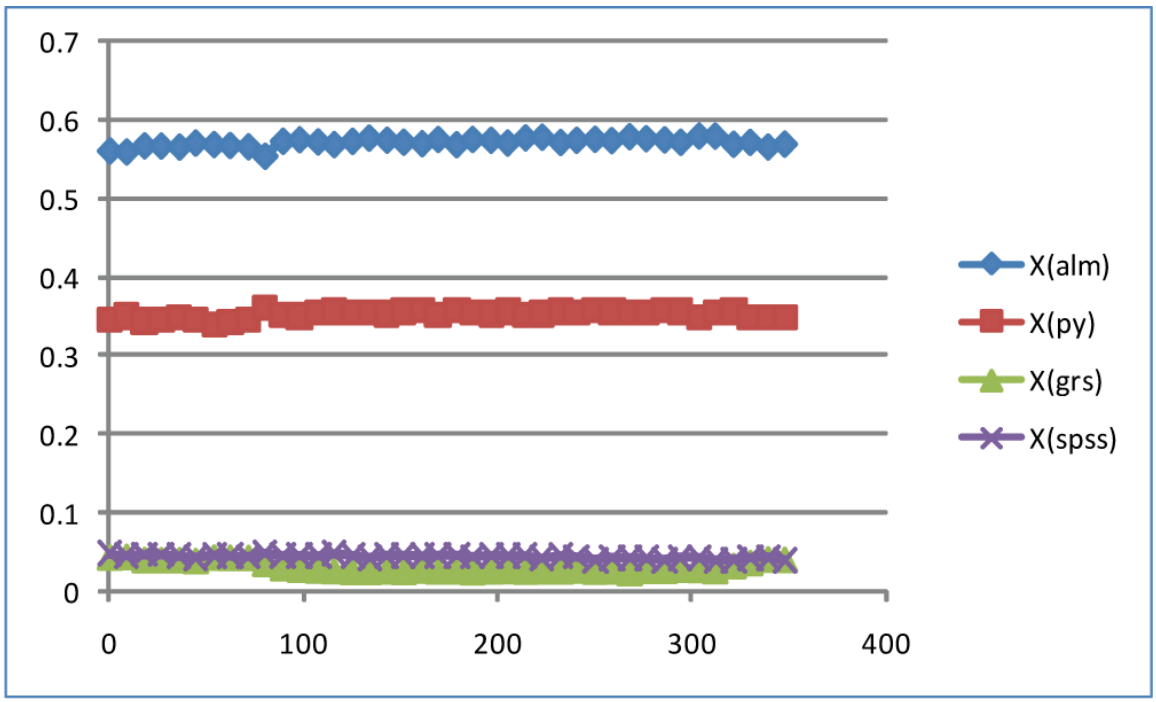

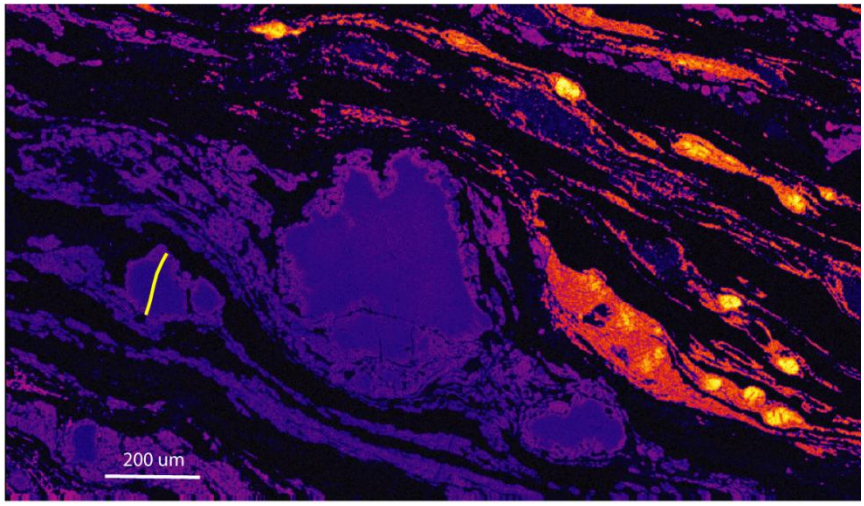

Figure 4

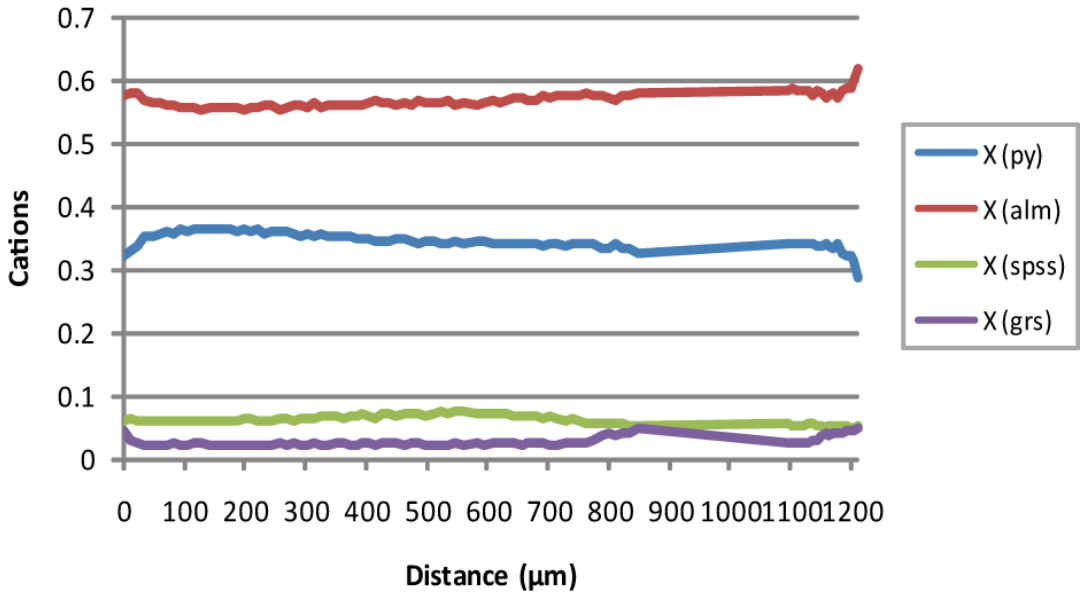
0.7
0.6
0.5
0.4
0.3
0.2
0.1
0
Cations
0 100 200 300 400 500 600 700 800 900 1000 1100 1200
Distance (µm)
X (py)
X (alm)
X (spss)
X (grs)

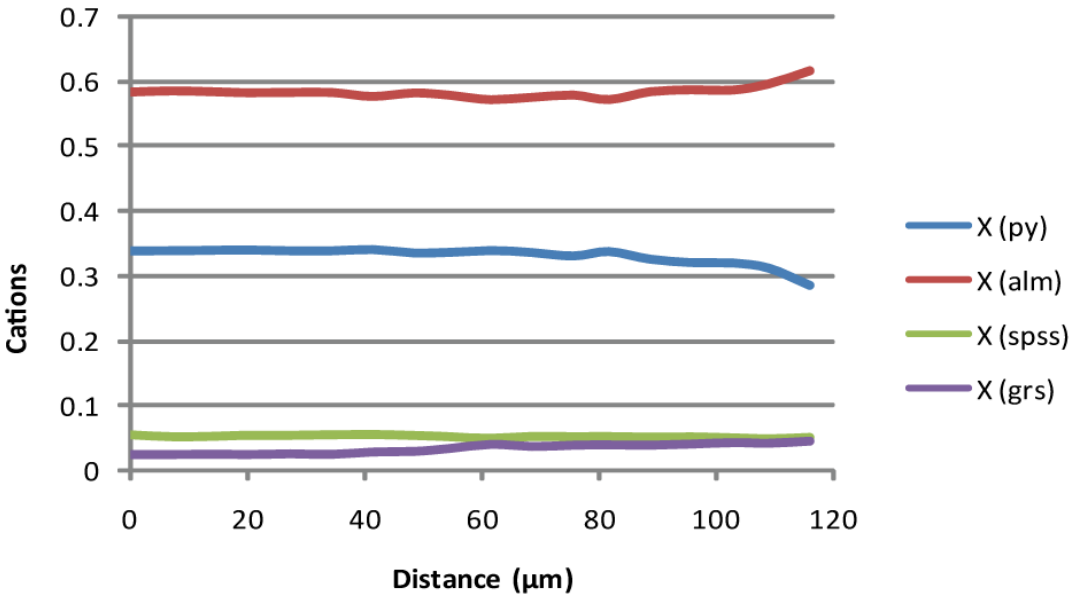
0.7
0.6
0.5
0.4
0.3
0.2
0.1
0
Cations
0 20 40 60 80 100 120
Distance (µm)
X (py)
X (alm)
X (spss)
X (grs)

Figure 4

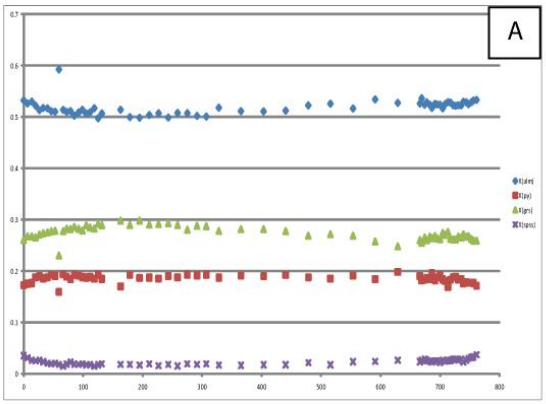

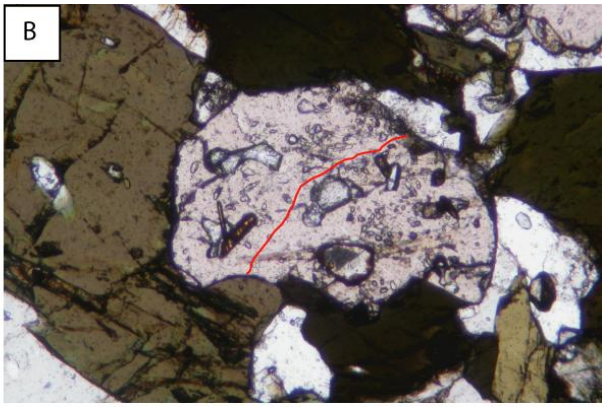

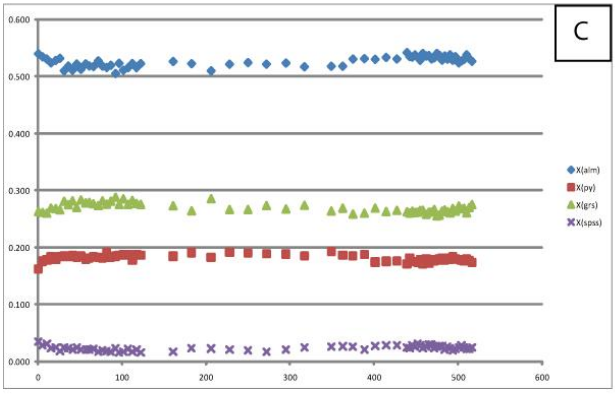

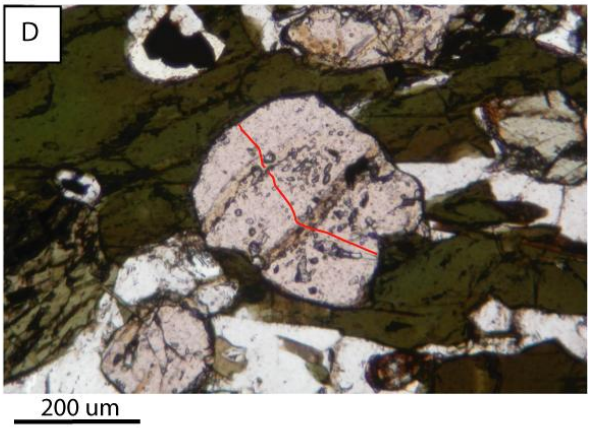

Figure 4

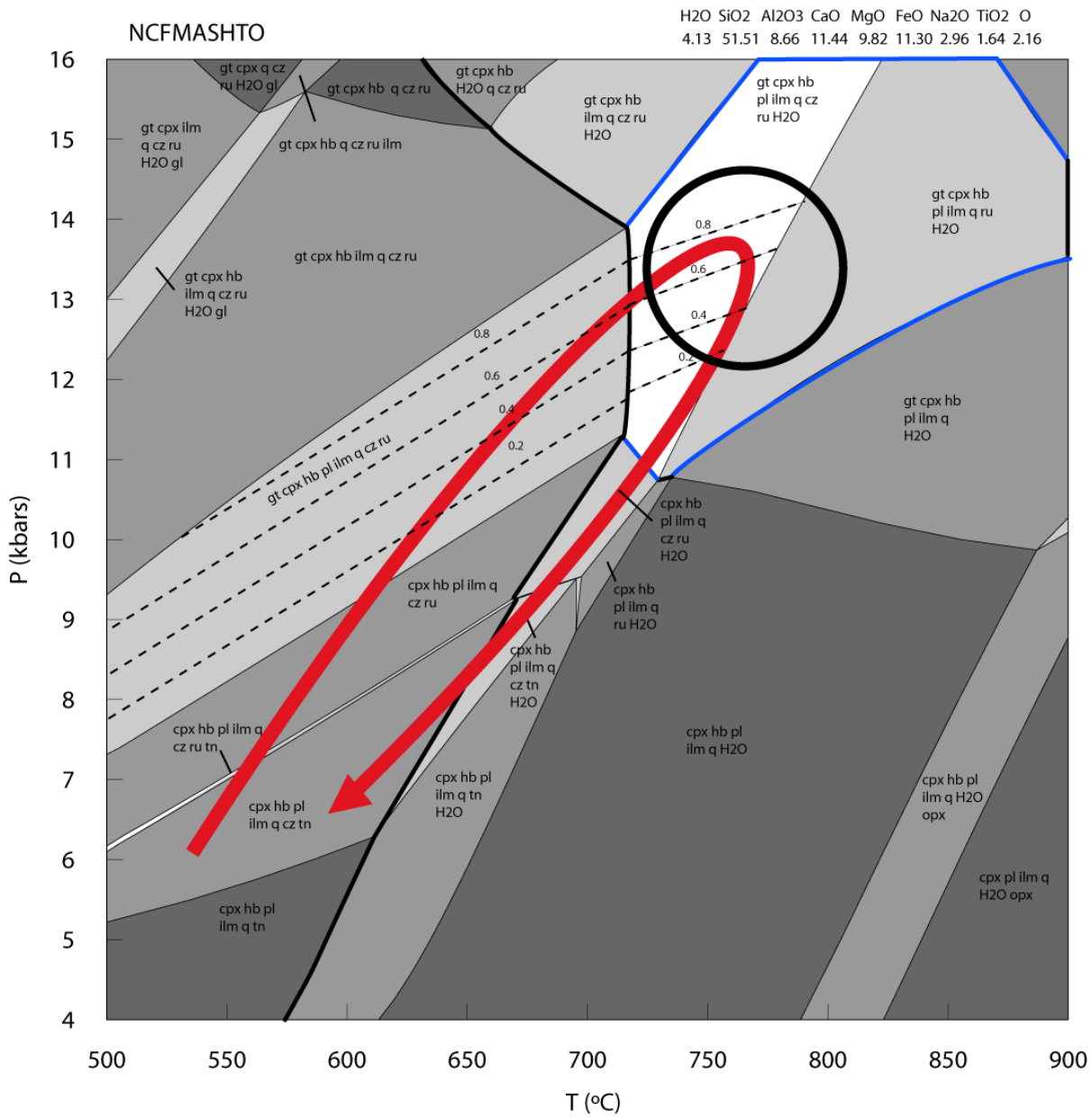
NCFMASHTO
H2O SiO2 Al2O3 CaO MgO FeO Na2O TiO2 O
4.13 51.51 8.66 11.44 9.82 11.30 2.96 1.64 2.16
gt cpx q cz ru H2O gl
gt cpx hb q cz ru
gt cpx hb H2O q cz ru
gt cpx hb ilm q cz ru H2O
gt cpx hb pl ilm q cz ru H2O
gt cpx ilm q cz ru H2O gl
gt cpx hb q cz ru ilm
gt cpx hb ilm q cz ru
gt cpx hb pl ilm q ru H2O
gt cpx hb ilm q cz ru H2O gl
0.8
0.6
0.4
0.2
gt cpx hb pl ilm q cz ru
gt cpx hb pl ilm q H2O
cpx hb pl ilm q cz ru H2O
cpx hb pl ilm q cz ru
cpx hb pl ilm q ru H2O
cpx hb pl ilm q cz tn H2O
cpx hb pl ilm q cz ru tn
cpx hb pl ilm q H2O
cpx hb pl ilm q cz tn
cpx hb pl ilm q tn H2O
cpx hb pl ilm q H2O opx
cpx hb pl ilm q tn
cpx pl ilm q H2O opx
P (kbars)
T (°C)
16
15
14
13
12
11
10
9
8
7
6
5
4
500
550
600
650
700
750
800
850
900

Figure 5

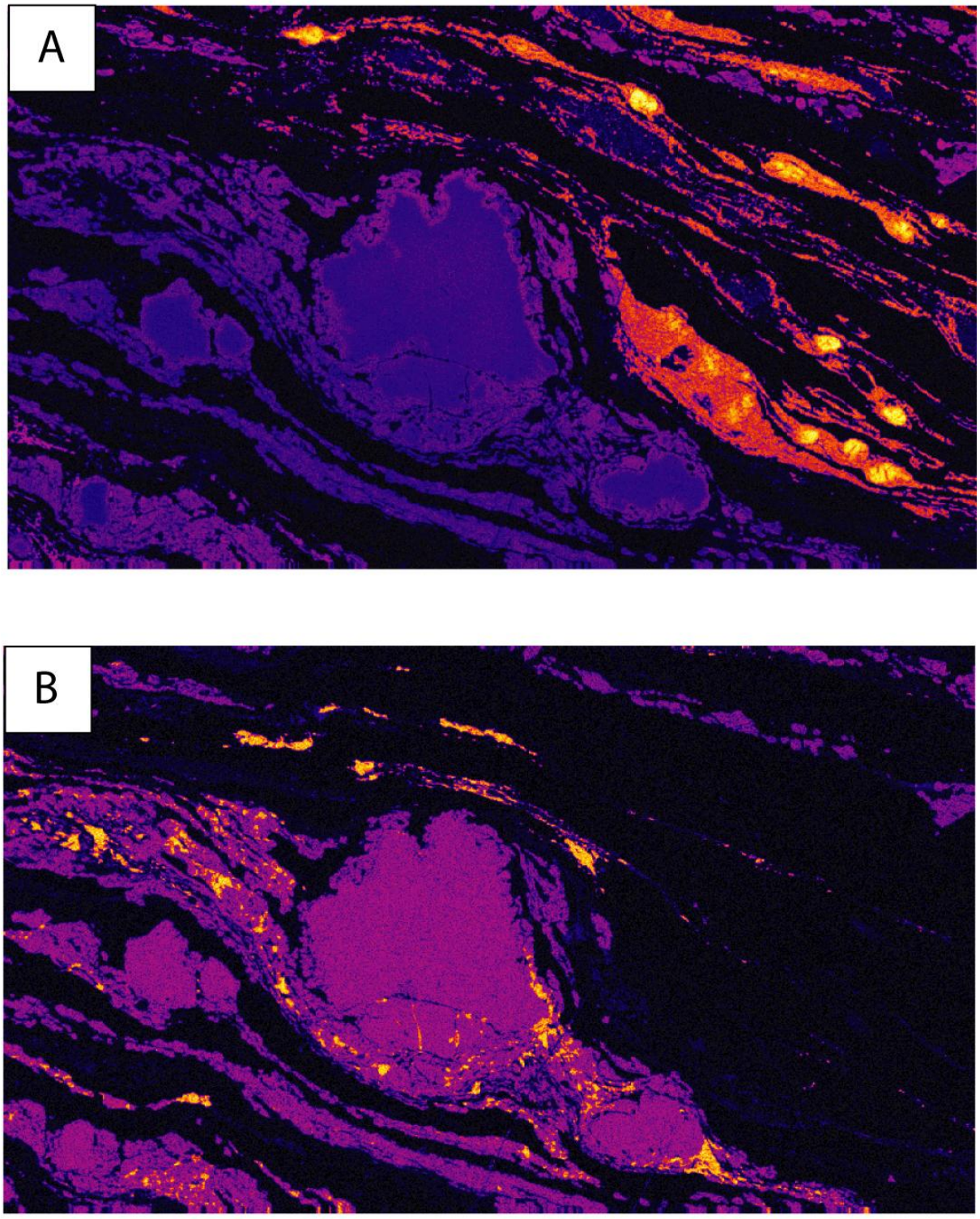

Figure 6

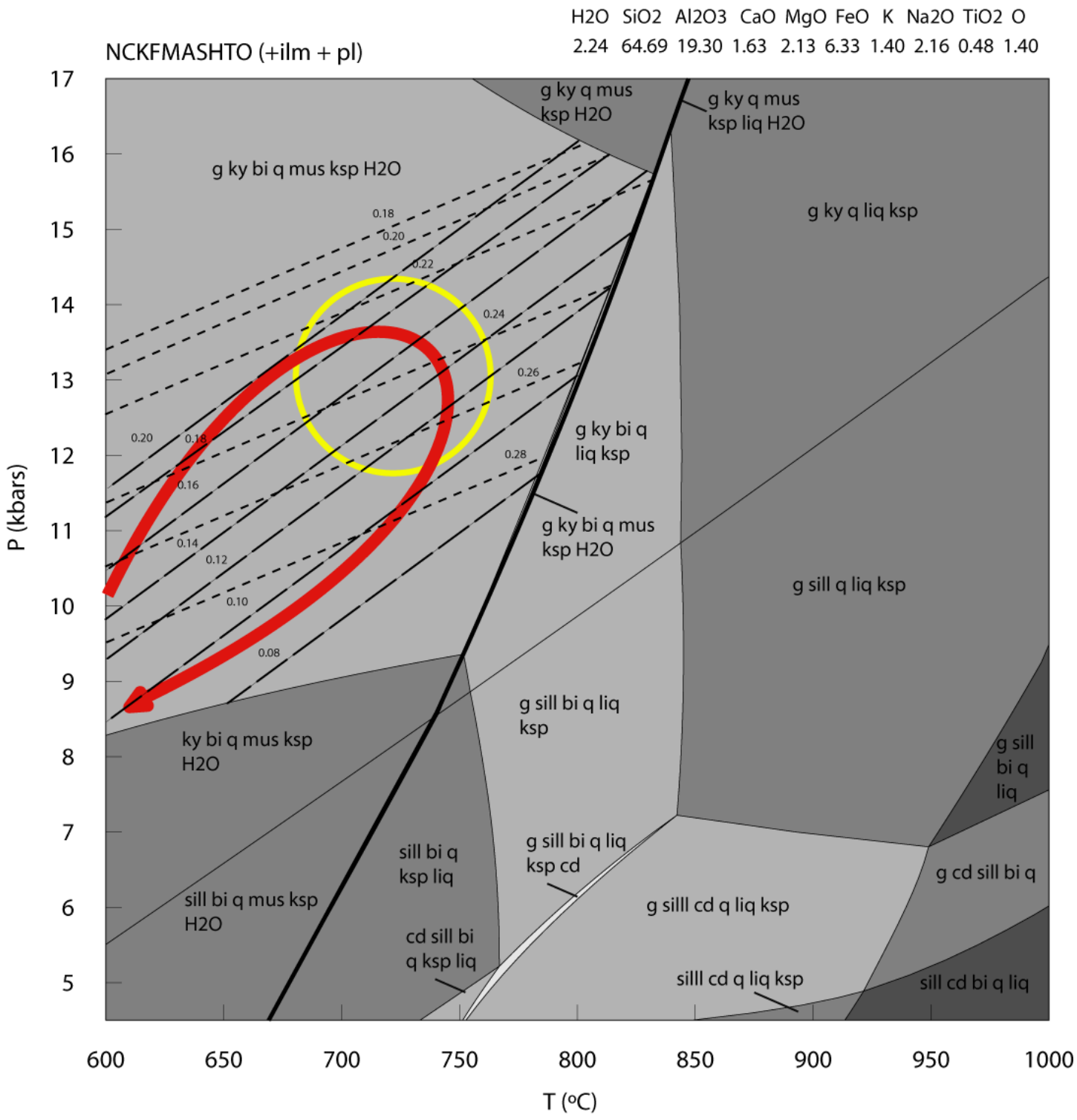
H2O SiO2 Al2O3 CaO MgO FeO K Na2O TiO2 O
2.24 64.69 19.30 1.63 2.13 6.33 1.40 2.16 0.48 1.40
NCKFMASHTO (+ilm + pl)
g ky q mus ksp H2O
g ky q mus ksp liq H2O
g ky bi q mus ksp H2O
g ky q liq ksp
g ky bi q liq ksp
g ky bi q mus ksp H2O
g sill q liq ksp
g sill bi q liq ksp
ky bi q mus ksp H2O
g sill bi q liq
sill bi q ksp liq
g sill bi q liq ksp cd
g cd sill bi q
sill bi q mus ksp H2O
g silll cd q liq ksp
cd sill bi q ksp liq
silll cd q liq ksp
sill cd bi q liq
0.18
0.20
0.22
0.24
0.26
0.28
0.16
0.14
0.12
0.10
0.08
P (kbars)
T (°C)
17
16
15
14
13
12
11
10
9
8
7
6
5
600
650
700
750
800
850
900
950
1000

Figure 7

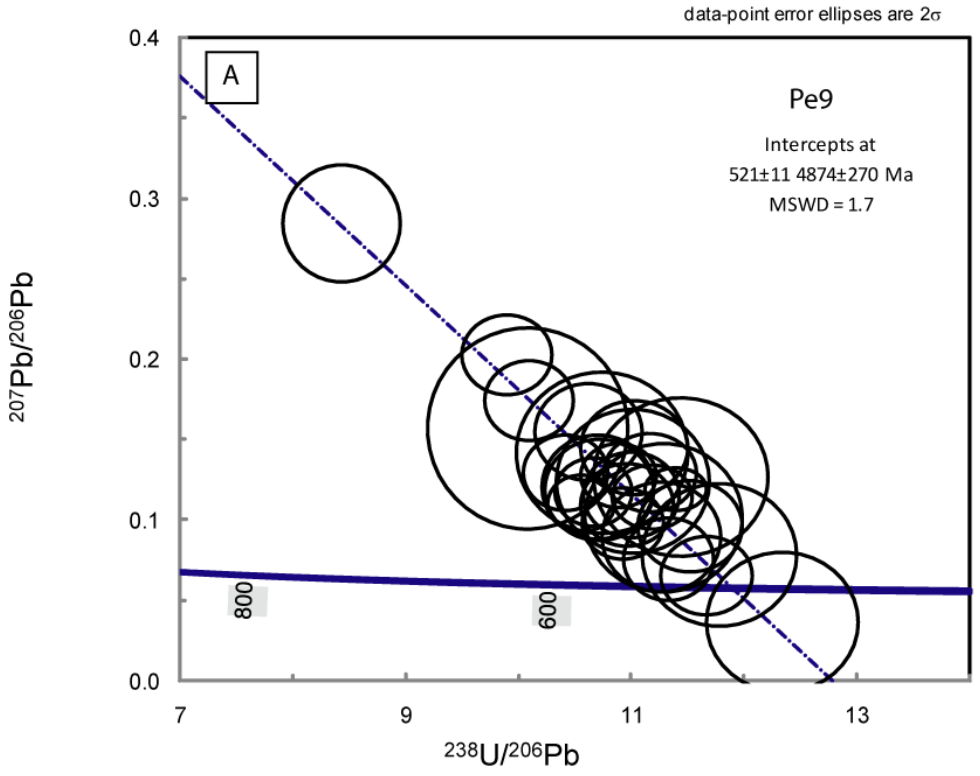
data-point error ellipses are 2σ
A
Pe9
Intercepts at
521±11 4874±270 Ma
MSWD = 1.7
800
600
0.4
0.3
0.2
0.1
0.0
7
9
11
13
207Pb/206Pb
238U/206Pb

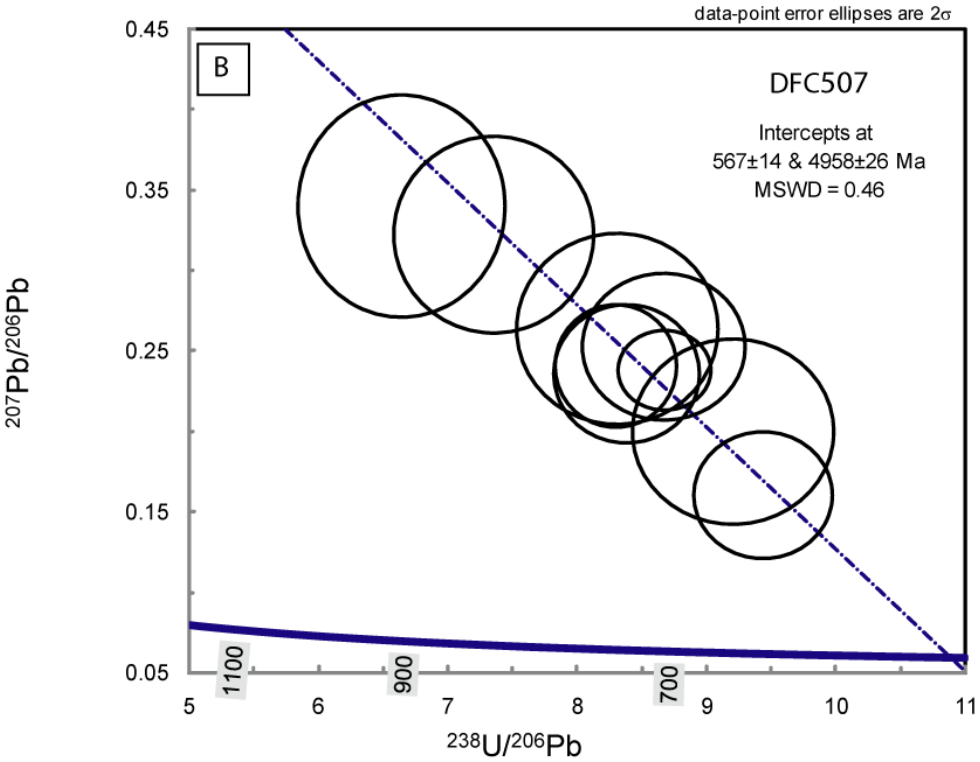
data-point error ellipses are 2σ
B
DFC507
Intercepts at
567±14 & 4958±26 Ma
MSWD = 0.46
1100
900
700
0.45
0.35
0.25
0.15
0.05
5
6
7
8
9
10
11
207Pb/206Pb
238U/206Pb

Figure 8

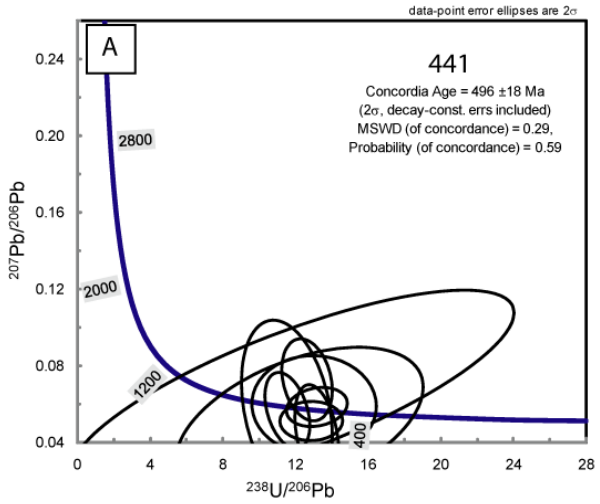
data-point error ellipses are 2σ
A
441
Concordia Age = 496 ±18 Ma
(2σ, decay-const. errs included)
MSWD (of concordance) = 0.29,
Probability (of concordance) = 0.59
2800
2000
1200
400
207Pb/206Pb
238U/206Pb

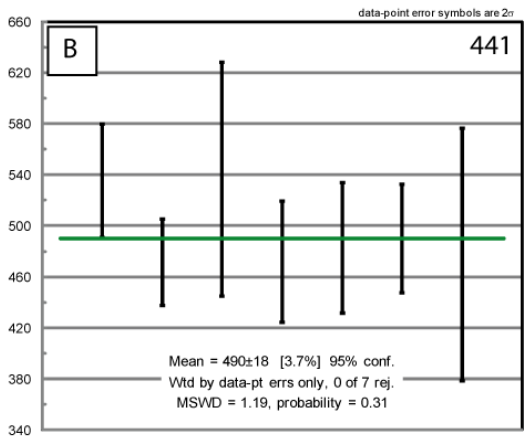
data-point error symbols are 2σ
B
441
Mean = 490±18 [3.7%] 95% conf.
Wtd by data-pt errs only, 0 of 7 rej.
MSWD = 1.19, probability = 0.31

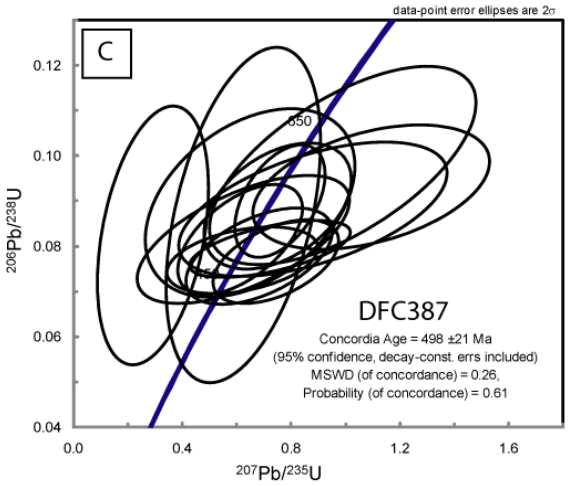
data-point error ellipses are 2σ
C
550
DFC387
Concordia Age = 498 ±21 Ma
(95% confidence, decay-const. errs included)
MSWD (of concordance) = 0.26,
Probability (of concordance) = 0.61
206Pb/238U
207Pb/235U

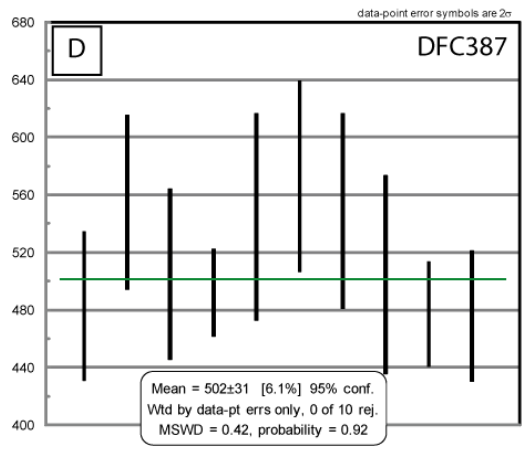
data-point error symbols are 2σ
D
DFC387
Mean = 502±31 [6.1%] 95% conf.
Wtd by data-pt errs only, 0 of 10 rej.
MSWD = 0.42, probability = 0.92

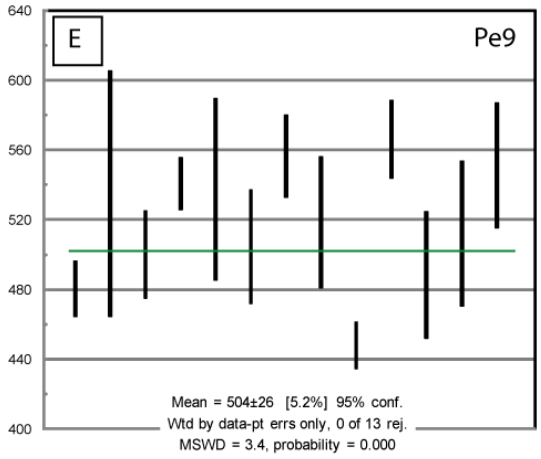
E
Pe9
Mean = 504±26 [5.2%] 95% conf.
Wtd by data-pt errs only, 0 of 13 rej.
MSWD = 3.4, probability = 0.000

Figure 9

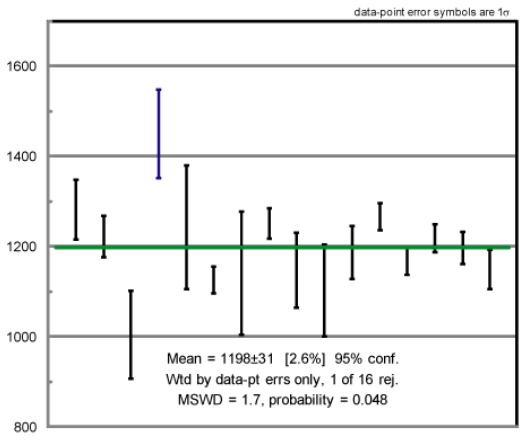
data-point error symbols are 1σ
1600
1400
1200
1000
800
Mean = 1198±31 [2.6%] 95% conf.
Wtd by data-pt errs only, 1 of 16 rej.
MSWD = 1.7, probability = 0.048

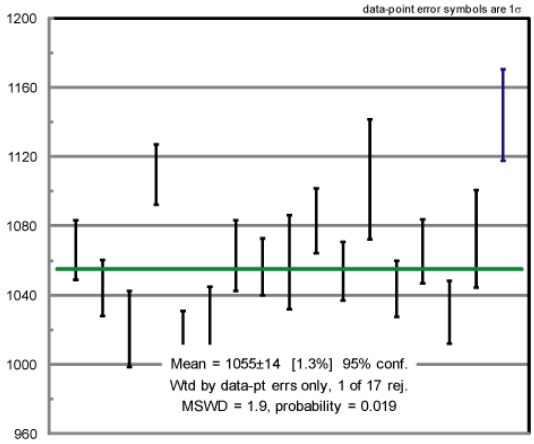
data-point error symbols are 1σ
1200
1160
1120
1080
1040
1000
960
Mean = 1055±14 [1.3%] 95% conf.
Wtd by data-pt errs only, 1 of 17 rej.
MSWD = 1.9, probability = 0.019

Figure 10

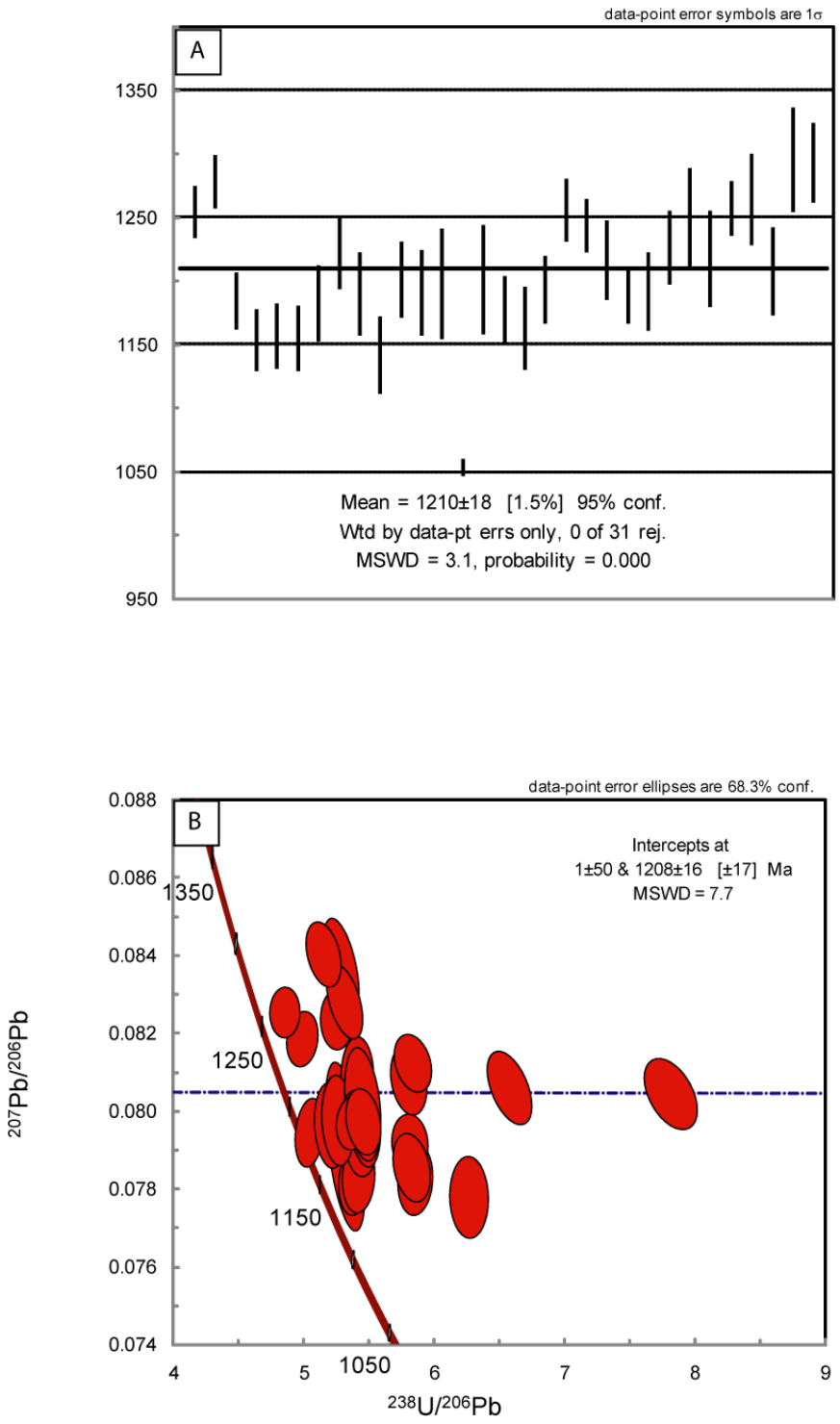
data-point error symbols are 1σ
A
1350
1250
1150
1050
950
Mean = 1210±18 [1.5%] 95% conf.
Wtd by data-pt errs only, 0 of 31 rej.
MSWD = 3.1, probability = 0.000
data-point error ellipses are 68.3% conf.
B
Intercepts at
1±50 & 1208±16 [±17] Ma
MSWD = 7.7
1350
1250
1150
1050
0.088
0.086
0.084
0.082
0.080
0.078
0.076
0.074
4
5
6
7
8
9
207Pb/206Pb
238U/206Pb

Figure 11

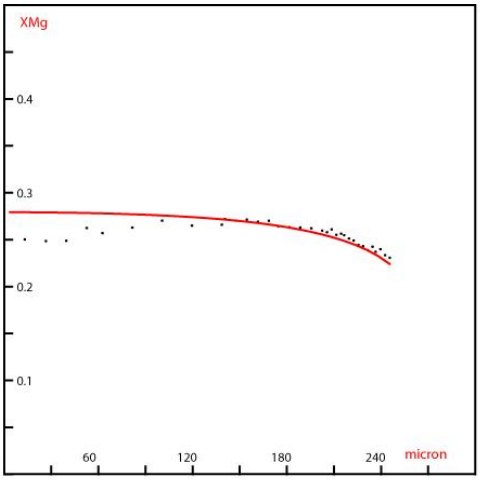

Distance from core

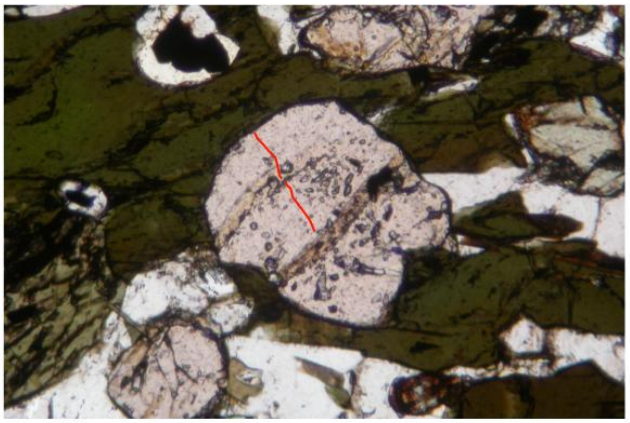

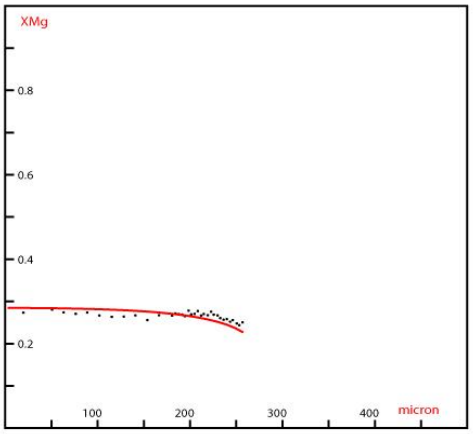

Distance from core

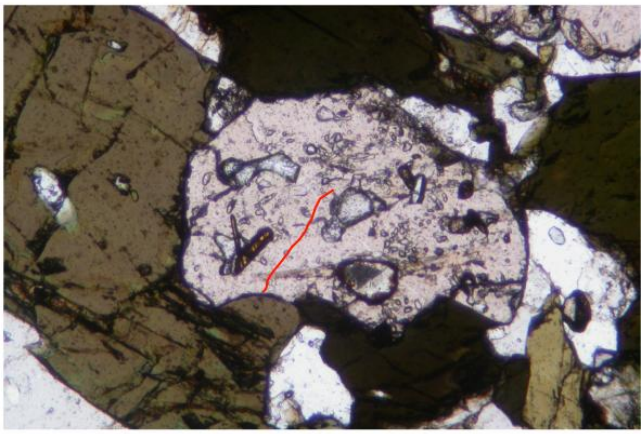

Figure 12

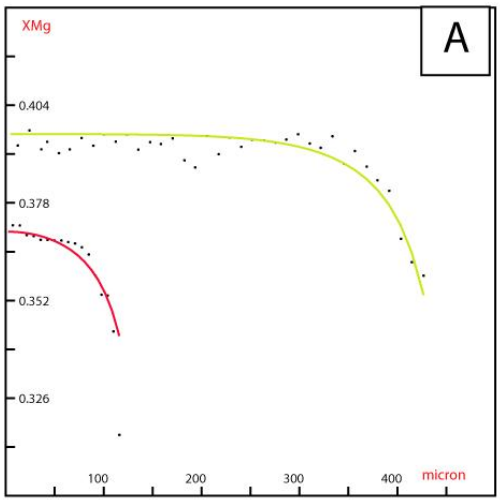

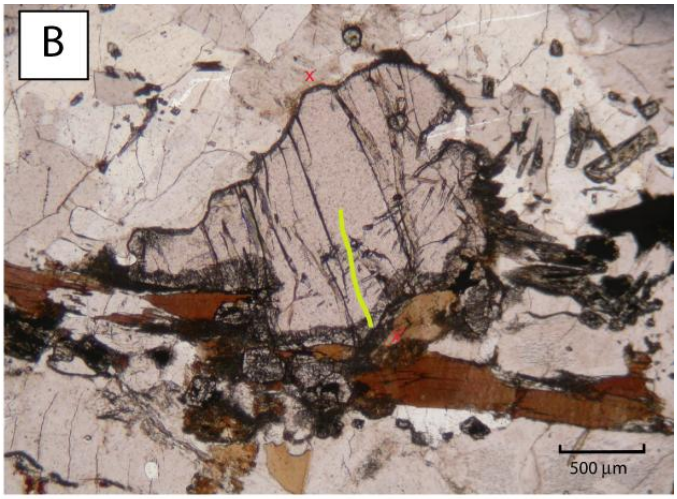

500 um

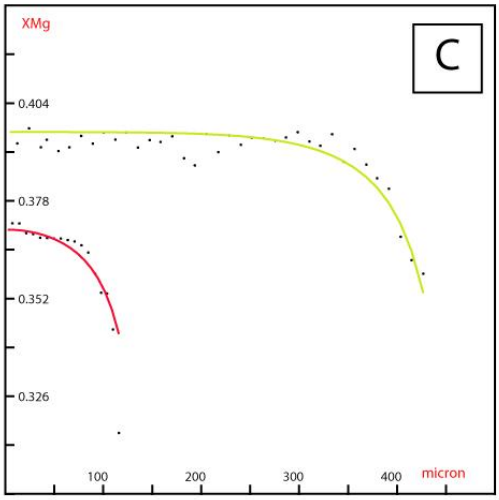

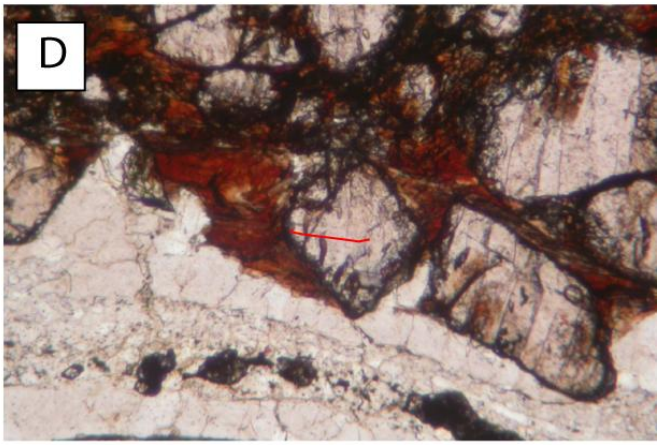

100 um

Figure 13